

THESIS

A NUMERICAL MODEL FOR THE DETERMINATION OF BIOMASS IGNITION FROM A
HOTSPOT

Submitted by

Patrick McArdle

Department of Mechanical Engineering

In partial fulfillment of the requirements

For the Degree of Master of Science

Colorado State University

Fort Collins, Colorado

Fall 2015

Master's Committee:

Advisor: John Williams

Xinfeng Gao

Patrick Shipman

Copyright by Patrick McArdle 2015

All Rights Reserved

ABSTRACT

A NUMERICAL MODEL FOR THE DETERMINATION OF BIOMASS IGNITION FROM A HOTSPOT

The determination of biomass ignition from an inert spherical hotspot using a fourth-order finite-volume method is presented. The transient ignition-combustion system is modeled by two coupled reaction-diffusion equations. One equation governs the heating characteristics of the biomass while the other governs the mass loss of the biomass. The combustion assumes a one-step, 1st-order Arrhenius reaction. This work is motivated and funded by the Department of Defense Legacy Program to create a munition specific fire danger rating system. Improving fire danger rating systems on military lands would minimize the economic and environmental impact of soldiers training on protected habitats. A better understanding of these ignition characteristics would also improve current fire spread models. Our result shows that given the ignition criteria derived from a simplified non-dimensional model and specifying critical values found by Gol'dshleger et al., an ignition probability can be established by varying the biomass properties based on moisture content. Following the procedure developed in this thesis, the computed ignition probabilities correlate well with experimental ignition data that was obtained at the Center for Environmental Management of Military Lands. Moreover, numerically solving the coupled reaction-diffusion system provides additional insight into more realistic ignition criteria involving mass loss. The numerical solution suggests more sources of heat loss, in addition to convection, must be considered for a more realistic ignition model.

ACKNOWLEDGEMENTS

Upon the completion of this thesis, I have had the luxury to reflect upon all of those in my life who have contributed to my academic success. More than anything, I want to emphasize my eternal gratitude to my family. Without my parents, brothers, grandparents, uncles, and aunts I would never have been able to pursue my academic ambitions. The continued support by my family has fueled my ambition and pushed me towards success that may otherwise not have been possible. For this reason, I dedicate this work to my family. In particular, a special dedication goes to my brother Robbie who, in his passing, taught me more about life than any other academic or professional pursuit will.

I would be remiss to not also acknowledge the friends I have known since high school as well as the friends I have come to know at Colorado State University. I would like to thank you all for helping me maintain a healthy perspective on my academic pursuits. During the most difficult times when I lost sight of the big picture I thank you all for bringing me back to reality.

Finally, I would like to acknowledge all the professors in the Mechanical Engineering department, the Mathematics department, as well as the Center for Environmental Management of Military Lands for their professional and academic support. Under your direction, I have grown more as a student and have developed many of the skills necessary that will allow for continued success academically and professionally.

This thesis is typeset in L^AT_EX using a document class designed by Leif Anderson.

TABLE OF CONTENTS

Abstract	ii
Acknowledgements	iii
List of Tables	vi
List of Figures	vii
Chapter 1. Introduction and Motivation	1
1.1. Introduction	1
1.2. Motivation and Objective	4
1.3. Approach and Outline	6
1.4. Biomass and Hotspot Characterization	8
Chapter 2. Theory and Models	22
2.1. Physical Model	22
2.2. Mathematical Model	23
2.3. Self-Heating and the Criteria for Thermal Explosion	24
Chapter 3. Numerical Modeling	33
3.1. Governing Equations	33
3.2. Finite Volume Method	36
3.3. Numerical Algorithm	43
Chapter 4. Results and Discussion	50
4.1. Numerical Results	50
4.2. Discussion	57

Chapter 5. Conclusion and Future Work.....	59
Bibliography.....	61

LIST OF TABLES

1.1	Elemental Composition of Biomass Types	9
1.2	Bomb Calorimeter Results	14
1.3	Cellulose, Hemicellulose, Lignin Content in Biomass.....	19
1.4	Biomass Thermal Properties	20
1.5	Hotspot Thermal Properties	21
4.1	Numerical Validation Parameter Values	50

LIST OF FIGURES

1.1	Cost of Fire in USA	4
1.2	Tracer Rounds.....	5
1.3	Common Biomass Types.....	9
1.4	CEMML Ignition Data	12
1.5	Effect of Moisture on Specific Heat.....	14
1.6	Thermogravimetric Data for Longleaf Pine.....	18
1.7	Thermal Conductivity of Cellulose	19
2.1	Sketch of the Physical Model	23
2.2	Critical Frank-Kamenetskii Values	29
2.3	Dimensionless Thermal Explosion Solution.....	29
2.4	Correlation to CEMML Ignition Data.....	31
3.1	Spherical Coordinates.....	34
3.2	Computational Domain.....	35
3.3	Cartesian grid for the biomass interior.....	45
3.4	Hotspot-Biomass Boundary	47
3.5	Biomass-Ambient Environment Boundary.....	49
4.1	Validation - Constant Temperature Hotspot.....	51
4.2	Validation - Constant Heat Flux Hotspot	52
4.3	Validation - Initial Temperature Hotspot	52

4.4	Validation - Constant Heat Flux Hotspot	53
4.5	Ignition Example	55
4.6	Non-Ignition Example	55
4.7	Effect of Q on Ignitions.....	56
4.8	Non-Ignition Solution Convergence.....	57

CHAPTER 1

INTRODUCTION AND MOTIVATION

1.1. INTRODUCTION

To understand biomass ignition it is important to first review what is required for combustion to occur. Generally speaking, in order for biomass to combust four primary components, heat, fuel, oxidizer, and uninhibited chemical reactions must be satisfied simultaneously under some physical and chemical constraints. Depending on what fuel, oxidizer, heat source, and chemical reactions are present, combustion still may not be possible. Where by combustion we mean a high-temperature exothermic chemical reaction between the fuel and the oxidizer. To initialize combustion and thus create a possible self-sustaining fire, defined as a combustion event that produces heat and light, an amount of heat must be added to the fuel-oxidizer system. For example, in woodlands there is an abundance of biomass that is dry and full of chemical energy. On Earth, oxygen is also an abundant oxidizer. A wildfire can start if heat is provided to the system. Often natural events such as lightning strikes and volcanic activity act as sources of heat capable of initiating a fire. In addition, a range of unnatural causes including fireworks, cigarettes, arson, industrial accidents, and a wide variety of other human related causes provides the heat necessary to start fires.

Historically, wildfires have been classified as either ground fires, surface fires, or crown fires. This classification differentiates the types of biomass being burned. Ground fires involve the combustion of the organic material on the forest floor above the mineral soil. Surface fires are made up of fuels less than two meters high and involve most bushes, tall grasses, and small trees. Crown fires burn through the canopy of larger trees [1]. Often times crown fires release firebrands, burning particles of organic matter, into the atmosphere.

These burning particles often travel large distances and start new ground fires away from the primary fire perimeter. These fires are known as spot fires. A review of numerous firebrand studies by Eunmo Koo et al. [2] and a numerical study by Sardoy et al. [3] show that much progress has been made in understanding the behavior of these firebrands. However, one of the least understood areas in fire science is the mechanisms and conditions necessary for a firebrand to cause an ignition where it eventually comes to rest. Certainly, the propensity for a biomass ignition from a firebrand depends on, but is not limited to, the geometric parameters of the firebrand, the composition of the firebrand, as well as its thermal characteristics. Similarly, how the firebrand is embedded in the biomass as well as the geometry, composition, and thermal characteristics of the biomass play an equally important role in the subsequent ignition or non-ignition. Many environmental factors also play a part in allowing for biomass ignition from a firebrand such as wind speed, and relative humidity. In part, due to the complex interaction between the firebrand and the biomass it is in contact with, very little is actually known about the initial conditions required for biomass to ignite and ultimately evolve into self-sustained combustion. In the literature, according to Babrauskas [4] “there have been only limited theoretical attempts to predict ignition of various substrates upon which a small hot object may fall.” In general, most ignition studies have been primarily experimental in nature and thus produce results applicable to only confined conditions. For example, according to McAllister [5], “predicting crown fires is understanding the ignition of fuel particles, most ignition models are empirically derived and can only be applied in the conditions in which they were measured.”

If we consider other non-organic firebrands, which we refer to as hotspots, many more situations can be explored. Previous experimental work by Rowntree [6] and computational

experiments of Rallis [7] and Tse [8] all attempt to determine the ability for aluminum sparks from clashing high voltage electrical conductors to cause fires in the grasses beneath them. In similar work, Hadden et al. [9] allowed hot spherical particles of various diameters and initial temperatures to fall into a bed of cellulose, and they recorded outcomes of no ignition, smoldering ignition, and flaming ignition. In general, the study found a hyperbolic relationship between particle diameter and temperature. The smaller the particle diameter the larger the particle temperature was necessary for flaming and smoldering ignitions. Partially due to concerns in the accuracy of measurement for the particle temperature, Uban et al. [10] conducted a similar experiment in a different study which resulted in a similar qualitative relationship. A numerical model by Lautenberger and Fernandez-Pello [11] was developed in hopes of more accurately correlating with experimental results. In a more recent experimental study, Finney et al. [12] examined the potential of rifle bullets to ignite organic matter after impacting a hard surface. After a projectile is fired, a certain percentage of the projectiles kinetic energy is converted into thermal energy upon impact with a target. Depending on the trajectory of the projectile fragment, some fragments can land in organic matter at a fairly high temperature. In the experiments conducted, temperatures of about 550 – 800 °C were recorded in some cases. Finney et al. found that hot fragments of rifle bullets did cause ignitions in a fuelbed of peat. Furthermore, the study also concluded that the moisture content of peat strongly affected ignition potential. However, as Babrauskas points out, despite many attempts there has been virtually no experimental validation of the theoretical models and that the thermophysical data for the material being studied is lacking and the theoretical models that do exist are more qualitative than quantitative [4, 11].

1.2. MOTIVATION AND OBJECTIVE

In the United States, the economic losses attributed to fire prevention, protection, and mitigation amounted to about 2.1% of the gross domestic product in 2011, which equates to about 329 billion dollars as shown in Figure 1.1 [13]. One area where fires contribute to this economic loss as well as an environmental loss is on military lands. One of the largest causes of fire on military lands is due to small arms tracer rounds [14]. Tracer bullets are built with a small charge of magnesium or phosphorus that ignites and emits light when the bullet is fired from the weapon. Figure 1.2 contains a photograph of the trajectories

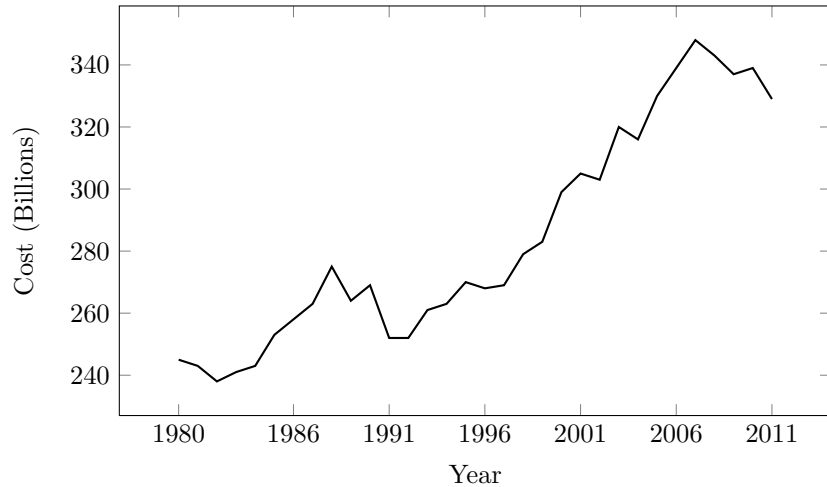


FIGURE 1.1. Cost of fire in the United States of America [13].

of tracer round bullets during a military training exercise. On the right side of the figure, the irregular trajectories show the bullets with tracers fragmenting and ricocheting off the target. The Department of Defense Legacy Resource Management Program has taken an interest in creating a munition specific fire danger rating system to prevent fires caused from projectiles used during military firearms training. To minimize the risk of starting forest fires on military lands, while simultaneously maximizing military training, a need for a more robust fire danger rating system is needed. This fire danger rating system ideally would be applicable to a wide variety of munitions and biomass characteristics. A method is desired

that determines how prone a munition is to starting a fire given certain fuel and munition characteristics. In general, current methods for determining what munition to train with and when is based largely on “gut instinct”; which often results in a particular munition being either over or under restricted. Military munitions are highly variable in terms of composition and fragment size. In addition, the environment and vegetation on military installations is highly variable. To create a munition specific fire danger rating system, it is not possible to



FIGURE 1.2. Tracer rounds fired during training. Photo credit: Sgt. Mike MacLeod.

rely on experiments alone. As a result, a predictive numerical model is needed to allow for a generalized biomass ignition criteria. As part of the Department of Defense Legacy Resource Management program, Beavers et al. at the Center for Environmental Management of Military Lands (CEMML) at Colorado State University obtained data relating the moisture content found in longleaf pine, cheatgrass, and smooth brome to its probability of ignition. The focus of this thesis is to develop a numerical model that ultimately correlates with the data collected by CEMML and is also robust enough to handle different munition fragment and biomass properties. By developing a numerical, physics-based model, steps can then be taken to produce a munition and biomass specific fire danger rating system. When training

in the field, this fire danger rating system can provide a metric that allows soldiers to train with weapons least likely to start fires under the given environmental conditions.

1.3. APPROACH AND OUTLINE

1.3.1. APPROACH. In the introduction it is clear that in the study of organic and inorganic firebrands coming into contact with biomass there are several basic elements that change under different conditions over a period of time. Namely, the heat transfer from the hotspot to the biomass, the exothermic heat release of the biomass, the heat diffusion through the biomass, and the heat losses for the hotspot as well as the biomass. One model of interest to this thesis work is known as hotspot theory, which characterizes ignitions from hot objects [6, 7, 15–17]. Hotspot theory has been applied with varying degrees of success to a variety of ignition problems [9–11]. The theoretical work of Gol'dshleger [18], a pioneer in hotspot theory, also correlated fairly well with experimental results given by Rowntree and Stokes as well as Hadden [6, 9]. Furthermore, Brindley and Weber [16, 17] cited applications to situations involving bulk powders that are handled by industrial equipment that can result in a localized hotspot within the powder due to mechanical friction. Hotspot theory can also be the basis for analyzing the characteristics of a firebrand and its ability to start spot fires.

Additional physics may also be accounted for in hotspot theory such as mass loss and oxygen diffusion. To make the problem more tractable, it is useful to first consider mass loss as the limiting factor for the energy generated by the biomass. Describing this system requires a solution to a coupled set of reaction-diffusion equations. One equation governs the heating characteristics of the biomass, while the other equation governs the mass loss. A spherical geometry is assumed for the hotspot and it is embedded perfectly in a concentric sphere of biomass. This study relies on the assumptions that the hotspot in contact with

the biomass is inert and at a higher temperature than the surrounding biomass, the hotspot is in perfect contact with the surrounding biomass and is transferred via conduction only, the biomass is able to release heat in an exothermic reaction as long as biomass is present, and the edge of the biomass away from the hotspot is cooled via convection to ambient air. The combustion assumes a one-step, 1st-order Arrhenius reaction for simplicity.

To gain insight on the problem of biomass ignition, we performed a numerical investigation. A computational study is advantageous due to the nature of the problem and the lack of existing theoretical or empirical biomass ignition models in the literature. Particularly, the numerical approach would allow for numerical experiments involving any combination of parameters that are associated with biomass fuel geometry and physical properties. Insight into how the parameters affect each other is important in developing more complex models and guiding future experimental work. To do this, first we explored the basic self-heating and thermal explosion theory that was originally introduced by Frank-Kamenetskii [19]. Next, we looked at the same explosion theory with the inclusion of a hotspot. By analyzing the heating characteristics associated with hotspot theory developed by Gol'dshleger, we developed a procedure to correlate with CEMML ignition data using a dimensionless thermal explosion model. Finally, a system of two coupled reaction-diffusion equations was solved using a 4th-order, finite-volume method to account for mass loss and more realistic ignition criteria.

1.3.2. **OUTLINE.** In this thesis, the remainder of this first chapter reviews and suggests parameter values for biomass that are used in this work. Within Chapter 2, the physical model of biomass ignition is simplified to a mathematical model of self-heating based on the work of Frank-Kamenetskii and Gol'dshleger. In Chapter 3, with the addition of mass loss

to the Frank-Kamenetskii model, a 4th-order finite-volume method is applied to solve the system of reaction-diffusion equations. Chapter 4 discusses the results and findings of this work. Finally, in Chapter 5 we conclude with the impact of this study on biomass ignition and propose future work.

1.4. BIOMASS AND HOTSPOT CHARACTERIZATION

All biomass is primarily composed of three things chemically, cellulose ($C_6H_{10}O_5$), hemicellulose, and lignin ($C_{40}H_{44}O_6$). In smaller parts, biomass also contains various amounts of mineral content, water, and other “extractives” that do not contribute to the overall structure of the biomass. In general, biomass encompasses all vegetation, alive and dead. Biomass fuel sources are categorized as either primary, secondary, or tertiary fuel sources. In established surface and crown fires, woody biomass, such as trees and large shrubs, becomes an important variable in the propagation of a forest fire. These fuel sources are referred to as secondary and tertiary fuel sources. Since we are concerned with the initial ignition, primary fuel sources on the forest floor associated with ground fires, such as grasses and pine needles, are considered. Fire ignition requires a primary fuel to be burnt first, thus heating up the surrounding secondary fuels and tertiary fuels. By vaporizing the water in adjacent biomass, the surroundings are preheated and ignite easier allowing for continued fire propagation. In general, this cascading process is limited by the fuel that is hardest to ignite. Ignition data from CEMML focused on three species that represent common biomass types that are found nationwide. The cheatgrass, longleaf pine, and smooth brome are shown in Figure 1.3 and all have a different biological structure. Nevertheless, it is important to remember that the defining characteristics between primary, secondary, and tertiary fuel sources does not differ greatly chemically. As we will see, the heating value of biomass can be estimated from known



(A) Cheatgrass

(B) Longleaf Pine

(C) Smooth Brome

FIGURE 1.3. Common Biomass Types. Photo Credit: Andrew Beavers.

values for carbon, hydrogen, oxygen, nitrogen, and ash content. Since the proportions of cellulose, hemicellulose, and lignin do not appear to vary greatly for biomass, certain property values, such as the heating value, are assumed to remain similar between these types of fuel sources. To give an idea of how similar different types of biomass are, an ultimate analysis table taken from Ragland [20] is provided. Table 1.1 shows that the primary components of biomass, carbon, hydrogen, and oxygen, do not differ greatly between biomass species. For reference, Table 1.3 shows the proportions of cellulose, hemicellulose, and lignin for several types of biomass.

TABLE 1.1. Ultimate Analysis (wt %) for Several Biomass Types [20]

Biomass	C	H	O	N	S	Ash
Oak	49.9	5.9	41.8	0.3	0	2.1
Pine	51.4	6.2	42.1	0.1	0.1	0.1
Switchgrass	47.4	5.8	42.4	0.7	0.1	3.6
Sudan grass	45.0	5.5	39.6	1.2	0	8.7

1.4.1. MOISTURE CONTENT. To begin a study of biomass ignition, an understanding of how moisture content affects the properties of biomass is needed. Generally, for a biomass particle undergoing a combustion process there are three stages of mass loss to be considered: drying, pyrolysis, and char combustion. To observe flaming combustion, pyrolysis must occur in the presence of oxygen to create a flame. For the purposes of this thesis work it will be

assumed that pyrolysis occurs after the biomass is dry. Nevertheless, it is suspected that drying and pyrolysis may actually occur to some degree simultaneously [4, 20]. The drying process is strongly affected by the heat of vaporization and how water is held within biomass. Water may exist in biomass as either a vapor, free liquid within the pores of the biomass, or adsorbed (chemically bound) water within the cellular structure of the biomass. The fiber saturation point (FSP) is the point at which water is no longer adsorbed into the biomass, but instead must be taken on as free water in the physical structure of the biomass. For biomass, the fiber saturation point is typically found to be around a moisture content of 30 – 35%. For most fires, it was suggested that the maximum moisture content that would start a fire for dead grasses is 15 – 20% and 25 – 30% for pine needles [4]. Moisture content directly affects the ignitibility of biomass. A hot object capable of vaporizing the moisture held within the biomass is key to starting an ignition. It is important to determine how much energy is required to dry the biomass sufficiently to allow for ignitions to occur. Ragland [21] stated that the “adsorbed water is held with increasing energy as the wood moisture content decreases.” This relationship is given by,

$$h_{sorp} = 0.4h_{fg} \left(1 - \frac{\mu_b}{\mu_{FSP}}\right)^2 . \quad (1)$$

Here, h_{sorp} is the heat of sorption, h_{fg} is the latent heat of vaporization for water, μ_b is the moisture content of the bound water, and μ_{FSP} is the moisture content at the fiber saturation point. According to Equation (1), as bound water content decreases, the water is held with increasing energy. As a result, particularly at low moisture contents, the heat of sorption must be taken into account. In our case, a sustained ignition only occurs if dry fuel, that is currently burning, releases enough energy to vaporize most of the moisture in

the adjacent biomass. If there is enough energy to heat the biomass to a critical level where the reaction becomes exothermic, a combustion wave will continue throughout the fuelbed if conditions supplying adequate oxygen permit. The moisture content of biomass can be measured on a wet or dry basis by

$$\mu_{wet} = \frac{m_{water}}{m_{water} + m_{dryfuel}} 100, \quad (2)$$

$$\mu_{dry} = \frac{m_{water}}{m_{dryfuel}} 100. \quad (3)$$

In these equations, μ_{wet} is the moisture content on a wet basis, μ_{dry} is the moisture content on a dry basis, m_{water} is the mass of the water, and $m_{dryfuel}$ is the mass of the dry biomass. Equation (3) indicates that in biomass the moisture content can be over 100% when looked at on a dry basis. Although much is known about the importance of moisture content, according to Babrauskas [4], “all of the information on moisture contents needed to achieve a sustained ignition is unfortunately anecdotal and systematic research is absent.”

Andrew Beavers et al. at the Center for Environmental Management of Military Lands at Colorado State University conducted hundreds of experiments to determine how the probability of ignition for the biomass varies with moisture content. The previously unpublished ignition data, reproduced with permission by Andrew Beavers et al., is pictured in Figure 1.3. In the experiments, a nichrome wire was heated to approximately 1000 °C and dropped into a tray with the loosely packed biomass for a duration of one second. If the biomass burned to the edge of the tray after the timed exposure to the hot spot, then an ignition was recorded. By doing a statistical analysis on the data collected, Andrew Beavers et al.

developed the following equations relating moisture content to the probability of ignition.

$$\text{Longleaf Pine : } P_{ig}(\mu) = e^{5.34-0.62\mu}/(1 + e^{5.34-0.62\mu})$$

$$\text{Cheatgrass : } P_{ig}(\mu) = e^{7.29-0.42\mu}/(1 + e^{7.29-0.42\mu})$$

$$\text{Smooth Brome : } P_{ig}(\mu) = e^{10.45-0.93\mu}/(1 + e^{10.45-0.93\mu})$$

Here, P_{ig} denotes the probability of ignition and μ denotes the fuel moisture content. By plotting the ignition probability equations in Figure 1.4, the effects of moisture content on the ignition of longleaf pine, cheatgrass, and smoothbrome is clear. As the moisture content increases the probability of ignition for these biomass species decreases.

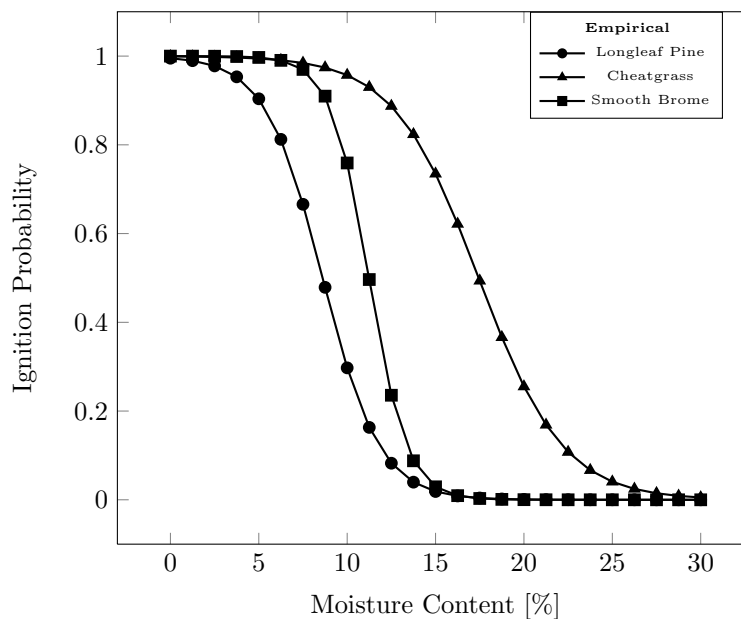


FIGURE 1.4. CEMML Ignition Data for Longleaf Pine, Cheat Grass, Smooth Brome.

1.4.2. HEAT OF COMBUSTION. The heat of combustion is the energy release of a substance per unit of mass and it varies depending on whether the water in the combustion products is a liquid or gas. By definition, the higher heating value (HHV) of a substance

assumes that the water in the combustion products condenses in liquid form. On the other hand, the lower heating value (LHV) of a substance assumes that the water in the combustion products remains in gaseous form. In general, Ragland [20] found that the HHV of wood on a dry basis is typically in the range of 19 – 22 MJ/kg. Since moisture content will be accounted for, it is more informative to look at the LHV which assumes that the energy required to vaporize the water is not released as heat after the combustion event. Several researchers have found that there is a correlation between the HHV of biomass fuels and the ultimate analysis of the biomass. Noting that the HHV and LHV are in units of MJ/kg, one such correlation by Reed [21] is given by

$$\text{HHV} = 0.341C + 1.322H - 0.12(O + N) - 0.153A + 0.0686. \quad (4)$$

Where C, H, O, N, A are the weight percents of carbon, hydrogen, oxygen, nitrogen, and ash. The average error associated with Equation (4) for biomass was 1.6% [21]. If the percents of cellulose, hemicellulose and lignin are known for a particular species, Equation (4) may be used to estimate HHV for the material. The lower heating value for wet biomass is given by,

$$\text{LHV} = \text{HHV}(1 - \mu_{wet}) - (h_{sorp} + h_{fg})\mu_{wet}. \quad (5)$$

In order to determine experimentally the heating values for cheat grass, longleaf pine, and smooth brome, we used an IKA Calorimeter System C200 bomb calorimeter. The samples were oven dried and kept in a desiccator before being placed in the calorimeter to guarantee a moisture content close to zero percent. Two experiments were performed and the results are listed in Table 1.2. The results between the two experiments are in good agreement with each other, and also agree with the values reported in the literature for similar biomass.

TABLE 1.2. Bomb Calorimeter Results-Results should be close to the HHV of the material as materials were dried to a moisture content close to 0%

Fuel	Run 1	Run 2	Units
Longleaf Pine	20639	20461	J/g
Cheat Grass	18043	18334	J/g
Smooth Brome	17517	17272	J/g

1.4.3. SPECIFIC HEAT. The specific heat of a substance is the energy required for the temperature of that substance to be raised by one degree. As expected, the moisture content of a substance has a direct impact on this value for any type of biomass. Ragland [20] cited a study in which the specific heat of wood was determined by

$$c = \frac{0.1031 + 0.003867T + 4.19\mu}{1 + \mu} + (0.02355T - 1.32\mu - 6.191)\mu. \quad (6)$$

In the above equation, μ is the moisture content on a dry basis and T is the temperature in Kelvin. The units for Equation (6) are kJ/kg·K. By plotting Equation (6), Figure 1.5 shows that as moisture content increases the specific heat increases as well.

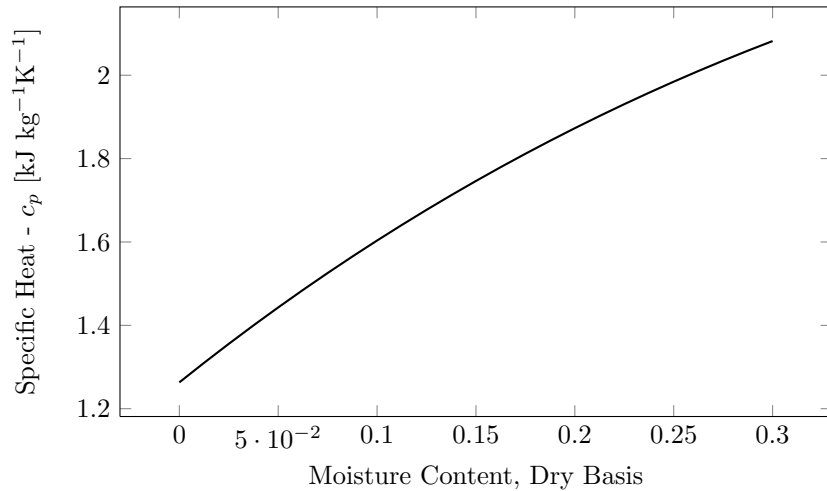


FIGURE 1.5. Specific Heat vs. Moisture Content at 300 K

According to a study by Dupont [22], the heat capacity for switchgrass at 313K was reported to be 1340 J/kg·K at a moisture content close to zero. This value is reasonably close to the value obtained from Equation (6).

1.4.4. ACTIVATION ENERGY AND PRE-EXPONENTIAL CONSTANT. The activation energy of a substance is the energy required to bring a material to a reactive state. Ragland [20] reports that a good initial estimate for most woods is approximately 129.704 KJ/mol, and suggested a value of $7 \times 10^7 \text{ s}^{-1}$ as the pre-exponential constant for wood. Jones [23] proposed that a value for the pre-exponential factor for sawdust to be $1.6 \times 10^5 \text{ s}^{-1}$. In separate work, Afzal [24] recorded activation energies of 139.94 kJ/mol, 197.14 kJ/mol, and 262.4 kJ/mol for three different species of pine needles. Thermogravimetric analysis is commonly used to determine the activation energy experimentally for a wide variety of substances. At CEMML, a thermogravimetric analysis was done to obtain the activation energy of longleaf pine, cheatgrass, and smooth brome. In this study, the Flynn-Wall method [25], also described in ASTM E1641-13 [26], is utilized to determine an approximate activation energy from experimental results. The Flynn-Wall method is briefly reviewed in the following analysis that was originally developed by Flynn et al. [25].

Assuming that α represents the degree of conversion from *solid* \rightarrow *product* and $f(\alpha)$ represents the conversion model, we may write

$$\frac{d\alpha}{dt} = \kappa f(\alpha). \quad (7)$$

The reaction rate constant, κ , is estimated using the Arrhenius equation,

$$\kappa = Ae^{-E/RT}.$$

For the purposes of this initial investigation, the degree of conversion may be defined as

$$\alpha = \frac{m_i - m_t}{m_i - m_f},$$

where m_i is the initial mass of the sample used in the experiment, m_f is the final mass and m_t is the mass of the sample at time t . Applying the chain rule,

$$\frac{d\alpha}{dT} = \frac{d\alpha}{dt} \frac{dt}{dT}, \quad (8)$$

and defining $\beta \equiv \frac{dT}{dt}$, the constant heating rate used in the experiment, then substituting Equation (8) into Equation (7), one can arrive at

$$\frac{d\alpha}{dT} = \kappa f(\alpha) \beta^{-1}.$$

Further substituting in the value of κ , we have

$$\frac{d\alpha}{dT} = \frac{A}{\beta} f(\alpha) e^{-E/RT}. \quad (9)$$

If $f(\alpha)$ is independent of T , and A and E are independent of both α and T , using separation of variables, Equation (9) can be integrated as follows,

$$\begin{aligned} F(\alpha) &= \int_0^\alpha \frac{1}{f(\alpha)} d\alpha = \frac{A}{\beta} \int_{T_0}^T e^{-E/RT} dT \\ &= \frac{AE}{\beta R} \left(\frac{e^{-E/RT}}{E/RT} + \int_{-\infty}^x \frac{e^x}{x} dx \right). \end{aligned} \quad (10)$$

Introducing

$$Z(E/RT) = \frac{e^{-E/RT}}{E/RT} + \int_{-\infty}^x \frac{e^x}{x} dx$$

Equation (10) can be simply written as

$$F(\alpha) = \frac{AE}{\beta R} Z. \quad (11)$$

Taking the \log_{10} of Equation (11), the relation becomes

$$\log_{10} F = \log_{10} \left(\frac{AE}{R} \right) - \log_{10} \beta + \log_{10} Z. \quad (12)$$

Applying an approximation used by Flynn-Wall [25], Equation (12) may be approximated as

$$\log_{10} F \cong \log_{10} \left(\frac{AE}{R} \right) - \log_{10} \beta - 2.315 - 0.457 \frac{E}{RT}. \quad (13)$$

Now, differentiating Equation (13) we arrive at the following relation for E,

$$\frac{d \log_{10} \beta}{d \frac{1}{T}} \cong \frac{0.457}{R} E. \quad (14)$$

Using Equation (14) and thermogravimetric data from the biomass samples heated at a constant rate, it is now possible to approximate the activation energy, E .

For the calculations, three conversion levels in the experimental thermogravimetric data were used at heating rates of 1°C/min, 3°C/min, 5°C/min, 10°C/min to create the Arrhenius plot of heating rate versus temperature. As an example, the experimental data gathered by thermogravimetric analysis for the longleaf pine needles is exhibited in Figure 1.6. It is clear from the figure that there is a linear relationship between the logarithm of the heating rate and the inverse temperature. In this case, averaging the slopes of these lines the activation energy was approximately 176 kJ/mol for longleaf pine.

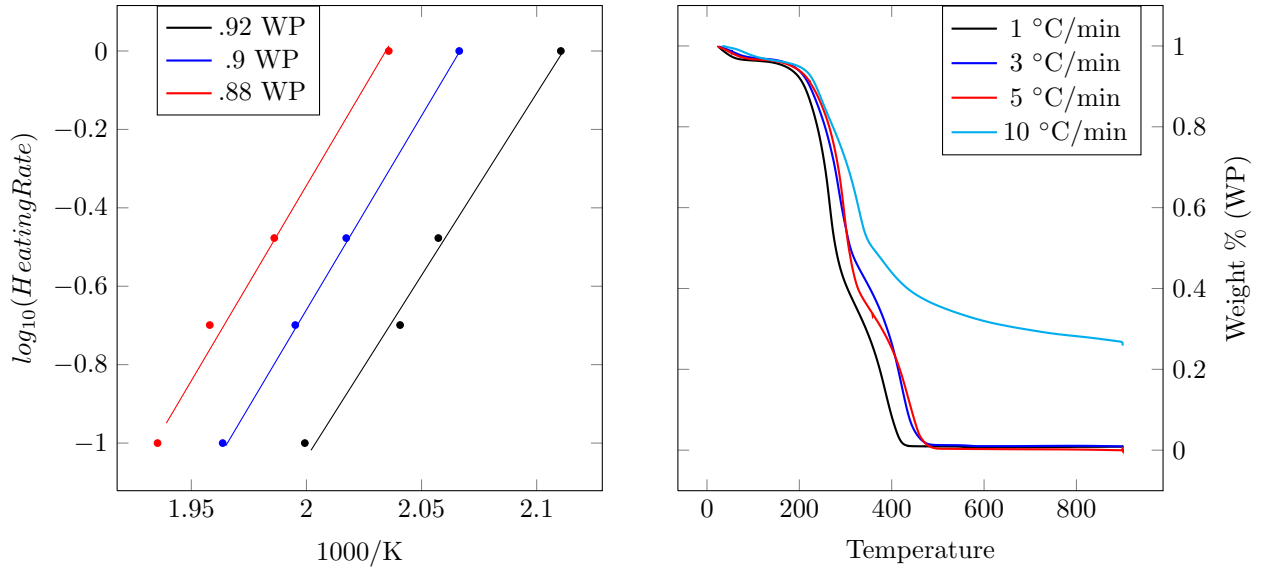


FIGURE 1.6. Thermogravimetric Data for Longleaf Pine.

1.4.5. THERMAL CONDUCTIVITY. The thermal conductivity of a material is a measure of its ability to transfer heat. For cellulose, Babrauskas [4] cited the following relationship, which works well as a first approximation

$$k = e^{1.45 \times 10^{-3} \rho - 3.39} . \quad (15)$$

Table 1.3 clearly shows that across a variety of biomass species, the amount of cellulose in biomass is greater than both lignin and hemicellulose. Since cellulose plays a major role in the biological structure of common biomass, the thermal conductivity Equation (15) will be used in the present study. Figure 1.7 plots the thermal conductivity over a range of density values common to most biomass species.

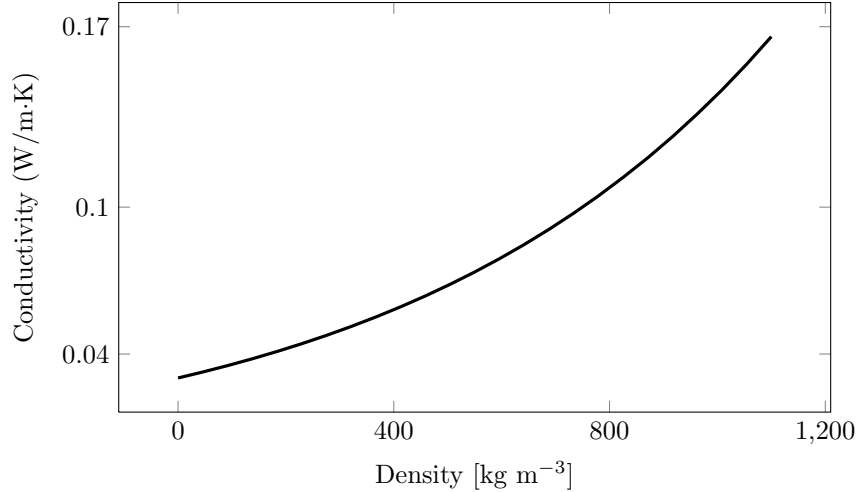


FIGURE 1.7. Estimation for the thermal conductivity of cellulose.

TABLE 1.3. Weight % Cellulose, Hemicellulose, Lignin from McKendry [27]

Biomass	Lignin(%)	Cellulose(%)	Hemicellulose(%)
Softwood	27-30	35-40	25-30
Hardwood	20-25	45-50	20-25
Wheat straw	15-20	33-40	20-25
Switchgrass	5-20	30-50	10-40

1.4.6. DENSITY. The bulk density biomass can be measured as a function of the biomass's geometry, composition, orientation, moisture content, and individual biomass particle density. It has been shown that the loosely packed bulk density ranges from 49 – 266 kg/m³ for wheat and 24 – 111 kg/m³ for straw grass. If these biomass types are packed, the bulk density ranges from 68 – 288 kg/m³ for wheat and 37 – 130 kg/m³ for straw grass [28]. Ragland [20] proposed ranges of bulk density for sawdust and wood shavings ranging from 157 – 227 kg/m³. Furthermore, Babraukas [4] tabulated the values of solid wood density ranging from 310 – 850 kg/m³. However, tropical hardwood species can have a measured density of 1040 kg/m³ [20]. In addition to all the variability listed above, the preparation used to prepare the biomass affects the overall bulk density. The fuels of interest in this study are assumed to be similar to wheat and straw grass. Santoni [29] measured three different pine needle

species and suggested densities ranging from approximately $446 - 808 \text{ kg/m}^3$. As a general rule of thumb Ragland [21] claims that the bulk density is approximately 40% of the particle density.

To summarize, the properties for biomass are highly variable and depend on the species and biological structure. Environmental factors, such as the relative moisture content and time of year, also effect the physical characterisitcs of biomass. Due to the extreme variability inherent in biomass, approximations for many of the parameter values is necessary. Since the literature does not report specific values for the biomass as shown in Figure 1.3, we use approximate values from the literature. Table 1.4 summarizes the parameter values for biomass that we use in our models.

TABLE 1.4. Approximate physical values for longleaf pine, cheatgrass, and smooth brome used in this study.

Fuel Parameter		Longleaf Pine	Cheatgrass	Smoothbrome
ρ [kg/m ³]	Density (Bulk)	650	115	115
Q [J/kg]	Higher Heating Value (HHV)	20.639×10^6	18.043×10^6	17.517×10^6
E [J/mol]	Activation Energy	201×10^3	65×10^3	65×10^3
k [W/m·K]	Thermal Conductivity	0.09	0.04	0.04

1.4.7. HOTSPOT. In this work, hotspots originate from military munitions that have been fired from a weapon. It is common that armed forces practice with weapons including flares, grenades, tracer munitions and a wide variety of rifle, pistol, and tank rounds. The different alloys of metal used to create these munitions and the possible geometries for the munition fragments is vast. For security purposes the military does not typically release this data. For civilian munitions, it is common that the bullets have cores made of steel or lead. These cores are then covered by an alloy of copper or steel.

Upon impact, the copper, steel, and lead fragment into many pieces. These pieces can be at high temperature and have the potential to land in ignitable biomass. Upon impact,

the kinetic energy of the munition is turned into heat and can cause fragments to reach temperatures capable of igniting organic material [12]. In military applications, some rifle rounds known as tracer rounds contain a mix of phosphorous or magnesium that burns at 600 – 1000 °C allowing the shooter to see the trajectory of the bullet [14]. The inclusion of this additional heat source causes the bullet and its fragments to reach higher temperatures upon contact with the biomass. Table 1.5 is a compilation of property values for copper, steel, and lead that can be used as hotspot parameters.

TABLE 1.5. Approximate thermal properties for some munitions from Incropera et al. [30].

Thermal Property	Conductivity [W/m·K]	Specific Heat [J/kg·K]	Density [kg/m ³]
Copper	401	390	8940
Steel (AISI 304)	14.9	477	7900
Lead	35.3	129	11340

CHAPTER 2

THEORY AND MODELS

2.1. PHYSICAL MODEL

To capture the full complexity of ignition phenomena in biomass, a great variety of physical considerations must be given. Figure 2.1, based on a more comprehensive solid and gas phase model proposed by Atreya [31], illustrates a wide range of physics commonly found in the combustion of solids. In the figure, a partially embedded hotspot heats the biomass through conduction. Volatile gases produced from heating the biomass then mixes with surrounding oxygen. If the hotspot is hot enough it can serve as a pilot and ignite the volatile gases into flaming combustion. The convection serves to cool both the biomass and the hotspot and also influences the oxygen diffusion into the biomass. Convection also has an effect on the volatile gas - oxygen ratio. Some physics not included in the figure is the moisture evaporation, radiation effects, as well as any convection within the biomass due to the volatile mass flow. Obviously, an ignition problem involving all possible physics can very quickly become intractable. Consequently, it is important to identify parameters that are most important in the problem that is presented and make assumptions allowing one to formulate a basic mathematical model.

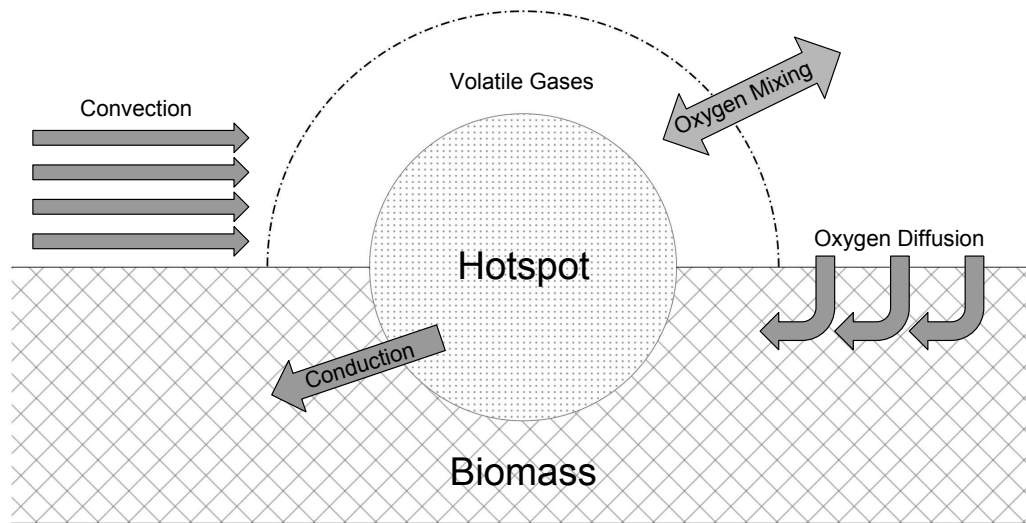


FIGURE 2.1. Physical considerations for ignition from a partially embedded hotspot.

2.2. MATHEMATICAL MODEL

The proposed mathematical model assumes drastic simplifications in contrary to the physical model proposed by Atreya [31]. First, our fuelbed is assumed to be composed of a homogeneous substance where porosity and other natural variations are neglected. Next, the combustion process of the fuelbed is assumed to follow one-step, 1st-order Arrhenius kinetics. Heat is transferred to the fuelbed via an inert, homogeneous particle by conduction only. The interface between the hotspot and the fuelbed is also assumed to be perfect. Furthermore, the heat loss to the environment is through convection only at the fuelbed-ambient environment interface. Restrictions to oxygen diffusion from the ambient environment into the fuelbed is also ignored. Throughout the combustion process all thermal property values remain constant.

2.3. SELF-HEATING AND THE CRITERIA FOR THERMAL EXPLOSION

Before introducing the equations governing a coupled reaction-diffusion model, it is important to understand a classical approach to ignition theory by the techniques of dimensional analysis. A simplified, non-dimensional model to analyze the transient, self heating characteristics of a substance that is exposed to an ambient temperature provides an excellent starting point. Originally studied by the Russian scientist Frank-Kamenetskii [19], several assumptions were made to understand ignition phenomena at a basic level.

- The geometry of the self heating substance is a slab, cylinder or sphere.
- The surface of the reactive substance is exposed to convection.
- Symmetry is perfect in every direction.
- Zero-order Arrhenius kinetics (No fuel depletion).
- Oxygen diffusion is ignored.
- Temperature gradients only occur in one direction.

In this analysis, the goal is to determine whether the rate at which heat is dissipated at the boundaries occurs fast enough to keep up with the energy generated within the fuelbed. The ability of the fuelbed to conduct heat to the boundary plays an important role on whether the heat generation dominates or not. If the heat generated is not conducted to the boundary fast enough, the temperature within the fuelbed will increase to infinity due to self-heating if the heat source does not go away over time. In one dimension, for a slab geometry, the transient heat diffusion equation with heat generation is described by

$$\rho c \frac{\partial T}{\partial t} = \rho Q A e^{-E/RT} + k \frac{\partial}{\partial r} \left(\frac{\partial T}{\partial r} \right). \quad (16)$$

In this problem we are interested in the system behavior after long periods of time. The goal is to determine whether, after a long time, a steady state is reached or a thermal explosion occurs and temperature approaches infinity. For a steady state, we may neglect the transient term and Equation (16) becomes

$$\rho Q A e^{-E/RT} = -k \frac{\partial}{\partial r} \left(\frac{\partial T}{\partial r} \right). \quad (17)$$

The boundary conditions are given by

$$\begin{aligned} -k \frac{dT}{dx} &= h(T_s - T_0), & \text{at } x = r, \\ \frac{dT}{dx} &= 0, & \text{at } x = 0. \end{aligned}$$

As outlined in “The Pi-Theorem” by Yarin [32], thermal explosion is classically explored by considering an ideally stirred reactor that is a closed volume filled with a homogeneous mixture of fuel and oxidizer (gaseous). Let the characteristic reactor size be r_0 . If we assume reactant concentrations are negligible before thermal explosion, the following parameters determine the local temperature within the reactor,

- Thermal Conductivity: $[k] = \text{JL}^{-1}\text{T}^{-1}\Theta^{-1}$
- Pre-Exponential: $[A] = \text{T}^{-1}$
- Activation Energy: $[E] = \text{Jmol}^{-1}$
- Universal Gas Constant: $[R] = \text{J}\Theta^{-1}\text{mol}^{-1}$
- Heat of Reaction (multiplied by ρ): $[Q] = \text{JL}^{-3}$
- Reactor Size: $[r_0] = \text{L}$
- Wall Temperature: $[T_0] = \Theta$

For the given parameters, J is the energy unit, L is the length unit, T is the time unit, and Θ is the temperature unit. From these parameters, the temperature can be written as a function of these variables

$$T = f(r, r_0, T_0, k, A, E, Q, R). \quad (18)$$

In order to reduce the number of variables that T is dependent on, Frank-Kamenetskii used an approximation for E/RT . Starting with the identity

$$\frac{1}{T} = \frac{1}{T_0} \left[1 - \left(\frac{T - T_0}{T_0} \right) + \left(\frac{T - T_0}{T_0} \right)^2 \frac{T_0}{T} \right], \quad (19)$$

if we assume $E/RT_0 \gg 1$ and $(T - T_0) \ll T$, multiplying Equation (19) by E/R we have

$$\frac{E}{RT} \approx \frac{E}{RT_0} - \frac{E}{RT_0^2} (T - T_0). \quad (20)$$

Using the approximation from Equation (20) the arrhenious equation can be written as

$$Ae^{\frac{-E}{RT}} \approx Ae^{\frac{-E}{RT_0}} e^{\frac{-E}{RT_0^2} (T - T_0)},$$

and we can define $\tilde{A} \equiv Ae^{\frac{-E}{RT_0}}$ and $\tilde{T}_0 \equiv RT_0^2/E$. From these defined parameters, we can now remove R and E from Equation (18), and T is now a function of

$$T = f(r, r_0, k, \tilde{A}, \tilde{T}_0, Q). \quad (21)$$

It is now straightforward to apply the Pi-Theorem to Equation (21). By choosing $\tilde{T}_0, \tilde{A}, k, r_0$ as repeating variables, the Pi-Theorem results in two Pi-groups. The first Pi-group is

$$\pi_1 = Q\tilde{T}_0^a \tilde{A}^b k^c r_0^d = \left[\frac{\text{J}}{\text{L}^3} \right] \left[\Theta \right]^a \left[\frac{1}{\text{T}} \right]^b \left[\frac{\text{J}}{\text{LT}\Theta} \right]^c \left[\text{L} \right]^d,$$

where $a = -1$, $b = 1$, $c = -1$, and $d = 2$. Traditionally, this Pi-group is commonly referred to as the Frank-Kamenetskii δ parameter and is given by

$$\delta = \pi_1 = \frac{Q\tilde{A}r_0^2}{\tilde{T}_0 k} = \frac{QEA r_0^2 \exp(-E/RT_0)}{RT_0^2 k}. \quad (22)$$

Physically, the Frank-Kamenetskii δ parameter is actually part of a larger group of dimensionless numbers known as Damköhler numbers, which are commonly written as $Da \equiv \text{ReactionRate}/\text{DiffusionRate}$. The second Pi-group is given by,

$$z = \pi_2 = r/r_0.$$

In addition, a non-dimensional temperature is introduced as,

$$\theta = \frac{E}{RT_0}(T - T_0).$$

Using these dimensionless numbers, the governing Equation (17) can be written as,

$$\frac{d^2\theta}{dz^2} + \frac{\kappa}{z} \frac{d\theta}{dz} = -\delta e^\theta \quad (23)$$

where $\kappa = 0, 1, 2$ for a slab, cylinder, or sphere. The boundary conditions are specified by,

$$\text{Bi}\theta + \frac{d\theta}{dz} = 0, \quad z = 1 \quad (24)$$

$$\frac{d\theta}{dz} = 0, \quad z = 0 \quad (25)$$

Here Bi is the Biot number which is the ratio of heat transfer from convection at the surface of the solid to the internal heat diffusion for the solid. Boddington [33] came up with an analytic approximation for the critical Frank-Kamenetskii δ parameter under these conditions,

$$\delta_c(\text{Bi}) = \left(\frac{1}{\delta_c(\text{Bi} \rightarrow \infty)} + \frac{e}{(j+1)\text{Bi}} \right)^{-1}, \quad (26)$$

where $j = 2, 1, 0$ for sphere, cylinder or slab geometries, $e = 2.718$ is the Euler's number, and the critical value $\delta_c(\text{Bi} \rightarrow \infty) = 3.32, 2.0, 0.88$ for a sphere, cylinder and slab [4, 33, 34]. The critical values for the bifurcation-point between steady and unsteady states, found by Boddington and given in Equation (26), are plotted in Figure 2.2 as a function of the Biot number. If the physical parameter values yield a δ value above the critical value, δ_c , thermal explosion occurs, temperatures go to infinity. Anything below the critical value allows for a finite temperature, while any δ equal to the critical value results in temperatures reaching infinity in an infinite amount of time. To more clearly show the effects of δ on Equation (23), a solution to the ordinary differential equation is required. By adding the transient term back into Equation (23), a solution was found using an ordinary differential equation solver in MATLAB. From the solution, Figure 2.3 shows the maximum temperature achieved as a function of time. For large biot numbers and a spherical geometry, δ_c is approximately 3.32, as predicted by Boddington [33], which is shown as the dashed curve. Any δ above

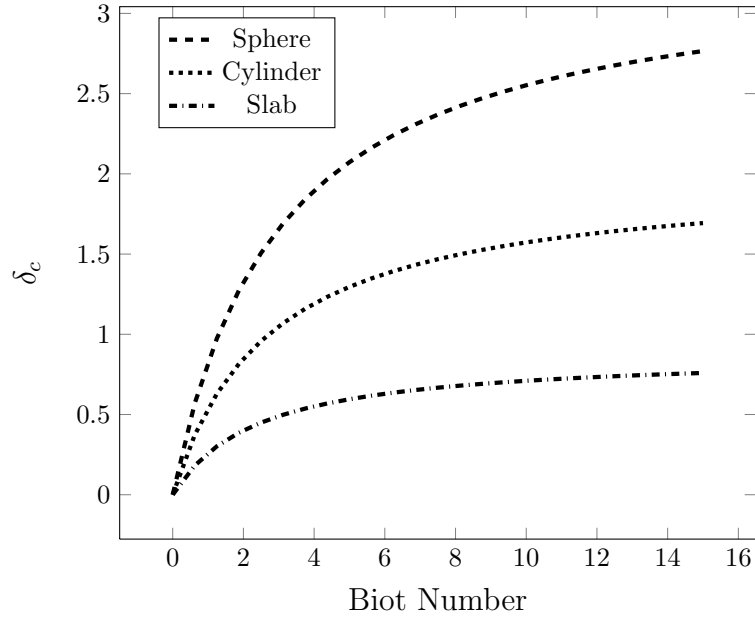


FIGURE 2.2. Critical δ_c in Frank-Kamenetskii's thermal explosion model for three geometries.

this value causes thermal runaway as exhibited by a sudden and large temperature increase.

For the Frank-Kamenetskii model, any δ above δ_c constitutes an ignition. For a situation

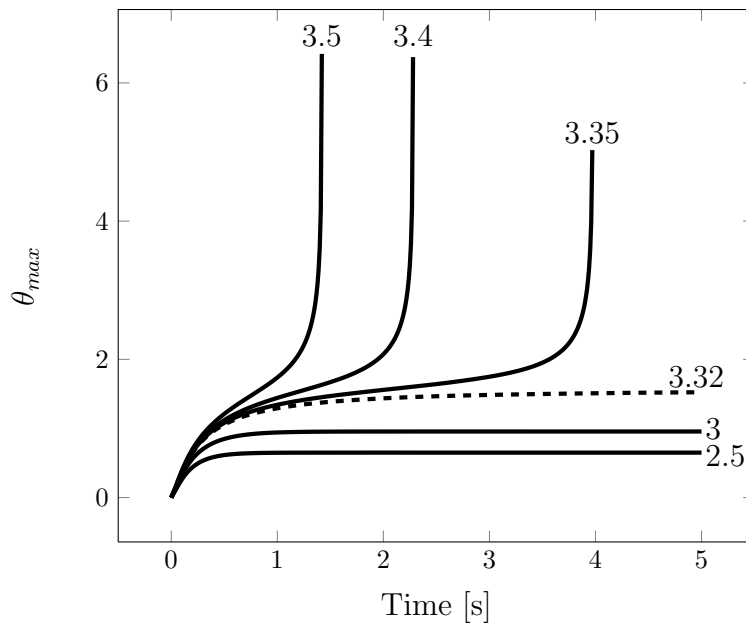


FIGURE 2.3. Affect of δ on maximum temperature for large biot numbers.

considered in this thesis work, a slightly more complicated analysis is required to account for the additional heat source – the hotspot.

Gol'dshleger [18] has shown that the thermal properties of the hotspot can also be taken into account to determine the critical δ_c parameter by use of the following equation

$$\delta_c = Z \left[1 + \frac{(\theta_h - 3)^2 \beta (j + 1)}{30 k_\lambda^{2/3} (1 + 3\beta^{2/3})} \right]^2, \quad (27)$$

where, $\beta = \frac{\rho C}{\rho_h C_h}$, $k_\lambda = \frac{k_h}{k}$, $\epsilon = \frac{RT_h}{E}$, $\delta = \frac{E}{RT_h^2} \frac{r^2 \rho Q A}{k} e^{-E/RT_h}$, $\theta_h = \frac{E}{RT_h^2} (T_h - T_0)$, and

$Z = 0.4(\theta_h + 2.25(j - 1))^2 (1 + 0.5\epsilon\theta_h) \sqrt{b^2 + 0.25j(j + 1)(b + 0.1b^3)}$. Gol'dshleger numerically

determined that this critical δ_c is only valid for the variables falling within the the range

$7.5 \leq \theta_h \leq 25$, $0.01 \leq \epsilon \leq 0.9/\theta_h$, $1 \leq k_\lambda \leq \infty$, and $0.05 \leq \beta \leq 10$. It is worth noting Linan

and Kindelan [4] came up with an alternative δ^{LK} analagous to the Frank-Kamenetskii δ . If

$\lambda_h \rho_h C_h \gg \lambda_0 \rho_0 C_0$,

$$\delta^{LK} = \frac{2RT_h^2 Q A r^2 \rho_0}{E(T_h - T_0)^2 \lambda_0} e^{-E/RT_0}.$$

The critical values are then given by,

$$\delta_c^{LK} = 1.15 + 1.32\Lambda^{-0.5} + 3.47\Lambda^{-1} + 0.302\Lambda^{-2},$$

$$\Lambda = \frac{RT_h^2}{(T_h - T_0)(j + 1)E} \frac{\rho_h C_h}{\rho_0 C_0}, \quad 10^{-2} < \Lambda < 10^3.$$

Nevertheless, for the purposes of this work we will focus on the critical value found by

Gol'dshleger. Despite the fact that the critical parameter defined by Gol'dshleger does not

take into account reactant depletion, it is possible to use this value to gain an idea on whether

or not an ignition will occur in the scenario where reactant is plentiful.

We developed a procedure that correlates with the probability plots shown in Figure 1.4 that were obtained experimentally by Andrew Beavers et al. at CEMML. The results of the procedure are pictured in Figure 2.4. This procedure consists of

- (1) Compute a range of δ values by varying the parameter values dependent on moisture content. Allow the moisture content to vary based on a Gaussian distribution with a small standard deviation around an average moisture content value. In this case, the average moisture content values vary between 0 – 30%.
- (2) Compare δ to δ_c . If $\delta > \delta_c$ then ignition occurs, if $\delta < \delta_c$ no ignition occurs.
- (3) Add up the number of δ 's that resulted in an ignition and divide by the total number of δ 's to get an ignition probability.
- (4) After running through average moisture contents up to 30% the pre-exponential constant was modified to make a better fit to the data. It may also be necessary to adjust the standard deviation if a correlation is still not found.

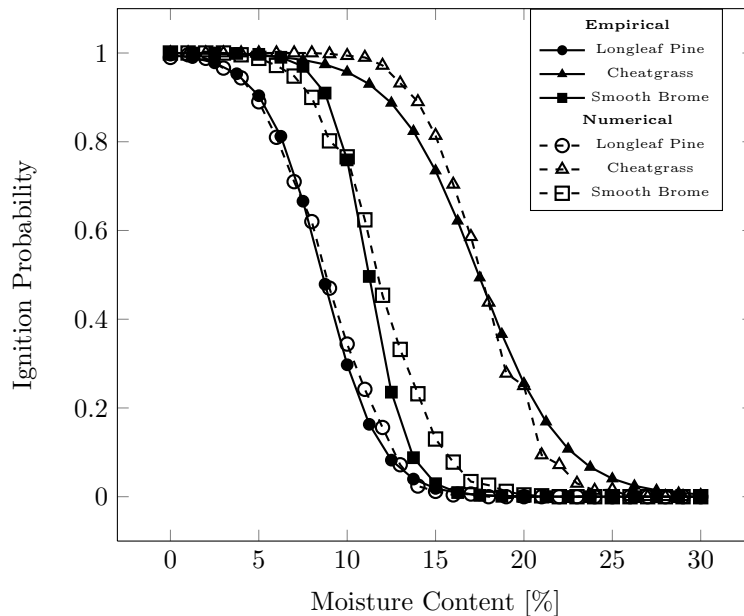


FIGURE 2.4. Comparison of experimental and numerical data from Gol'dshleger δ_c ignition criteria using our correlation procedure.

To make the correlation, several parameters including the pre-exponential constant and the standard deviation for the normal probability distribution were adjusted. A normal distribution with a small standard deviation, $\sigma = .08$, was used to reflect the fact that the fuelbeds are conditioned at a specific moisture content value and the amount of moisture in the fuelbed does not vary greatly from that conditioned value. Under controlled experimentation, a small standard deviation is a reasonable assumption since the moisture content in test fuelbeds can be conditioned uniformly. The pre-exponential constant was adjusted until a reasonable fit with the data was achieved. We found that a better fit to the data resulted in the pre-exponential constant $A \approx 3.3 \times 10^7 \text{ s}^{-1}$ for longleaf pine, $A \approx 1.55 \text{ s}^{-1}$ for cheatgrass, and $A \approx 1.4 \text{ s}^{-1}$ for smooth brome.

In the next chapters, we find that, if reactant consumption is taken into account, the criteria for ignition can be defined in a different way. More specifically, if mass loss is taken into account, an ignition criteria can be based on the amount of reactant left after a sufficiently “long” time period.

CHAPTER 3

NUMERICAL MODELING

3.1. GOVERNING EQUATIONS

Throughout this thesis, the term hotspot has been used to describe a hot spherical particle composed of some type of metal. In general, the hotspot may be modeled as having a constant temperature for a given time, constant heat flux for a given time, or an initial temperature. Physically, the hotspot is to be completely embedded within a self-reactive medium referred to as the fuelbed, which is composed of a cellulose based material or biomass, with properties as described in Section 1.4. Furthermore, the hotspot is said to have perfect contact with the fuel and thus the only mode of heat transfer considered at the hotspot-fuelbed interface is through conduction. Several studies by Brindley, Staggs, and Weber [15–17] have suggested that depending on the power of the hotspot, either a reaction front will be established and the fuel will be totally consumed or the fuelbed will only be partially consumed. If the fuel is fully consumed, we refer to the case as an ignition. If instead the fuelbed is only partially consumed or not consumed at all, the case is referred to as a non-ignition.

Francis-Pello et al. [11] concluded that the hotspot theory as described by Gol'dshleger is more qualitative than quantitative, because not enough physics is being captured by Gol'dshlegers simplified model. In an effort to make the ignition model more quantitative, the additional physics of mass loss is explored. In this thesis work we consider a set of coupled reaction-diffusion equations. They are given by the following governing equations,

$$\rho c \frac{\partial T}{\partial t} = \rho Q A M e^{-E/RT} + \frac{\partial}{\partial r} \left(r^2 k \frac{\partial T}{\partial r} \right), \quad (28)$$

$$\frac{\partial M}{\partial t} = -AMe^{-E/RT} . \quad (29)$$

Equation (28) governs the transient heating characteristics of the fuelbed, while Equation (29) governs the transient mass loss of the fuelbed. In these equations, T is the temperature, M is the mass fraction of the biomass, r is the radial ordinate, and t is the time. The other parameters include ρ the fuel density, c the specific heat of the fuel, k the thermal conductivity of the fuel, Q the heat of combustion, A the pre-exponential factor, E the activation energy, and R the universal gas constant.

3.1.1. COMPUTATIONAL DOMAIN. The domain of interest is the fuelbed and the solution will be for a spherical geometry as shown in Figure 3.1. Figure 3.2 illustrates the hotspot

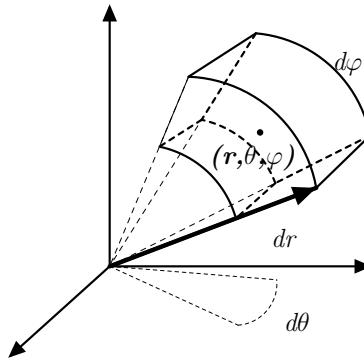


FIGURE 3.1. Spherical Coordinates and Control Volume.

and the domain of interest. If the radius of the hotspot is a , then the fuel bed is said to extend from $a \leq r \leq b$ where b is the outermost edge of the fuelbed in contact with the ambient environment. In the analysis of these coupled nonlinear partial differential equations, assuming perfect spherical symmetry, the problem may be analyzed as a one-dimensional problem in the radial direction. If the hotspot is small, temperature variations within the hotspot can be negligible and the cooling of the hotspot may be analyzed using a lumped capacitance approach. Furthermore, the center of the hotspot is treated as an adiabatic

surface. The hotspot is initially at a specified temperature of T_H . Note that in equations that involve parameters of the hotspot, subscripts H and f are used to distinguish between physical parameters for the hotspot and fuelbed.

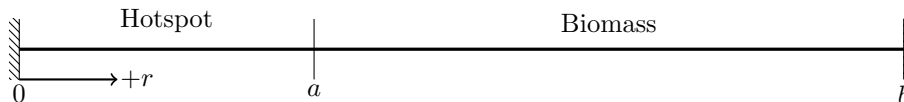


FIGURE 3.2. Computational Domain: $a \leq r \leq b$

From Equations (28) and (29), it is clear that several assumptions have been made. The fuel is self-reactive. In modeling combustion it is important to consider oxidizers since for all combustion processes $Fuel + Oxidizer \rightarrow Products$. However, assuming a self-reactive medium we ignore the contribution of the oxidizer to the combustion process. Furthermore, from this assumption we may also infer that during the combustion process one unit mass of fuel is converted directly to one unit mass of product. The fuel and product are also said to have the same thermal properties and they remain constant over time. Lastly, the fuelbed is assumed to be dry. Nevertheless, later iterations on the analysis of Equations (28) and (29) include the effects of moisture content by varying parameters, such as Q , to reflect the level of moisture content in the fuelbed. An ignition is said to have occurred if the mass fraction of the fuel bed $M \rightarrow 0$ as $t \rightarrow \infty$. On the other hand, an ignition has not occurred if $M \rightarrow (Nonzero\ Value)$ as $t \rightarrow \infty$ while the temperature of the fuel bed $T \rightarrow T_{ambient}$ as $t \rightarrow \infty$. The studies by Brindley and Weber [16, 17] focused on the analysis of a constant heat flux hotspot and how it affects the mass loss. The hotspot of interest in this work is one that has an initial temperature and cools as it transfers its heat to the fuelbed. The hotspot of this type was studied in greater detail by Staggs [15]. A boundary condition of

this type captures the basic physics of a hot bullet fragment landing in a cooler fuelbed of biomass.

3.1.2. BOUNDARY CONDITIONS. As stated in the previous section, this thesis work is primarily concerned with phenomena associated with a hotspot of a specified initial temperature. As a result, the boundary condition at the hotspot-fuelbed interface is governed by the transfer of heat from the hotspot to the fuelbed by means of conduction only. On the fuelbed-ambient environment interface a convective boundary condition is assumed,

$$\rho_H c_H \frac{\partial T}{\partial t} \Big|_{r=a} = \frac{\partial}{\partial r} \left(r^2 k_f \frac{\partial T}{\partial r} \right), \quad (30)$$

$$k \frac{\partial T}{\partial r} \Big|_{r=b} = h(T_\infty - T). \quad (31)$$

3.1.3. INITIAL CONDITIONS. Initially, both the hotspot and the fuelbed are set at specified initial temperatures. The fuelbed is initialized at a temperature that is equal to that of the surroundings and the hotspot is set at some temperature greater than ambient temperatures. More explicitly, the initial conditions are presented by,

$$T(r, 0) = \begin{cases} T_H & \text{at } r = a \\ T_\infty & \text{at } a < r \leq b \end{cases} \quad M(r, 0) = 1, \quad (32)$$

where T_∞ is ambient temperature.

3.2. FINITE VOLUME METHOD

We solve Equations (28) and (29) using the finite-volume method. They are rewritten in terms of conservative quantities. Since ρ and c are both constants and if we define the

internal energy to be $e = cT$ we may rewrite Equation (28) as

$$\frac{\partial(\rho e)}{\partial t} = \frac{\partial}{\partial r} \left(r^2 k \frac{\partial T}{\partial r} \right) + \rho Q A M e^{-E/RT} \quad (33)$$

Since M is a mass fraction we may multiply both sides of Equation (29) by the constant ρ

$$\frac{\partial(\rho M)}{\partial t} = -\rho A M e^{-E/RT}. \quad (34)$$

In spherical coordinates the del operator is given by,

$$\vec{\nabla}_s = \hat{r} \frac{\partial}{\partial r} + \frac{\hat{\theta}}{r} \frac{\partial}{\partial \theta} + \frac{\hat{\phi}}{r \sin \theta} \frac{\partial}{\partial \phi}.$$

For a given vector $\vec{F} = F_r \hat{r} + F_\theta \hat{\theta} + F_\phi \hat{\phi}$, the divergence in spherical coordinates may then be given by

$$\vec{\nabla}_s \cdot \vec{F} = \frac{1}{r^2} \frac{\partial(r^2 F_r)}{\partial r} + \frac{1}{r \sin \theta} \frac{\partial(F_\theta \sin \theta)}{\partial \theta} + \frac{1}{r \sin \theta} \frac{\partial F_\phi}{\partial \phi}. \quad (35)$$

Since we are only concerned with the radial direction and due to spherical symmetry, we may define $F_r = -k \frac{\partial T}{\partial r}$ while $F_\theta = F_\phi = 0$. Therefore, Equation (35) becomes

$$\vec{\nabla}_s \cdot \vec{F} = \frac{-1}{r^2} \frac{\partial(r^2 k \frac{\partial T}{\partial r})}{\partial r}.$$

Defining $f(T, M) = \rho Q A M e^{-E/RT}$ and $g(T, M) = -\rho A M e^{-E/RT}$ the governing equations are given by,

$$\begin{aligned} \frac{\partial(\rho e)}{\partial t} + \vec{\nabla}_s \cdot \vec{F} &= f(T, M), \\ \frac{\partial(\rho M)}{\partial t} &= g(T, M). \end{aligned}$$

Rewriting the governing equations into a vector form as

$$\frac{\partial \mathbf{U}}{\partial t} + \vec{\nabla}_s \cdot \mathbf{F} = \mathbf{P}. \quad (36)$$

In Equation (36) the solution vector, \mathbf{U} , flux vector, \mathbf{F} , and physical source vector, \mathbf{P} , are given by,

$$\mathbf{U} = \begin{bmatrix} \rho_f c_f T \\ \rho_f M \end{bmatrix}, \quad \mathbf{F} = \begin{bmatrix} -k \frac{\partial T}{\partial x} \\ 0 \end{bmatrix}, \quad \mathbf{P} = \begin{bmatrix} \rho_f Q A M e^{-E/RT} \\ -\rho_f A M e^{-E/RT} \end{bmatrix}.$$

We integrate Equation (36) and use the divergence theorem to arrive at

$$\frac{d}{dt} \int_V \mathbf{U} dV + \oint_S \mathbf{n} \cdot \mathbf{F} dS = \int_V \mathbf{P} dV. \quad (37)$$

For a cell of volume ΔV , the average value of \mathbf{U} and \mathbf{P} can be expressed as

$$\bar{\mathbf{U}} = \frac{1}{\Delta V} \int_{\Delta V} \mathbf{U} dV, \quad (38)$$

$$\bar{\mathbf{P}} = \frac{1}{\Delta V} \int_{\Delta V} \mathbf{P} dV. \quad (39)$$

With the above equation in mind, we will drop “-” for simplicity. By rewriting Equation (37) using Equations (38) and (39), we have

$$\Delta V \frac{d\mathbf{U}}{dt} + \oint_S \mathbf{n} \cdot \mathbf{F} dS = \Delta V \mathbf{P},$$

$$\frac{d\mathbf{U}}{dt} = \frac{-1}{\Delta V} \oint_S \mathbf{n} \cdot \mathbf{F} dS + \mathbf{P}.$$

Assuming a control volume, (i,j,k) ,

$$\frac{d\mathbf{U}_{i,j,k}}{dt} = \frac{-1}{\Delta V_{i,j,k}} \sum_{m=1}^{N_f} \mathbf{n}_{i,j,k,m} \cdot \mathbf{F}_{i,j,k,m} A_{i,j,k,m} + \mathbf{P}_{i,j,k} \quad (40)$$

where $\Delta V_{i,j,k}$ is the cell volume, N_f is the number of distinct faces on the cell volume, and $A_{i,j,k,m}$ is the area of the distinct face, and $\mathbf{n}_{i,j,k,m}$ is the outward normal vector of face m . In spherical coordinates $dV = r^2 \sin(\phi) dr d\theta d\phi$ and $dS = r^2 \sin(\phi) d\theta d\phi$. In our case, since we are only concerned with spherical coordinates in the radial direction the number of faces reduces to two. Furthermore, since our problem is one-dimensional, the subscripts j, k may be neglected. By assuming symmetry in the θ and ϕ directions ΔV for some cell i can be expressed as,

$$\Delta V_i = \iiint r^2 \sin(\phi) dr d\theta d\phi = 4\pi \int_{r_L}^{r_R} r^2 dr = \frac{4\pi}{3} (r_R^3 - r_L^3) \quad (41)$$

Where for simplicity $(r + \frac{\Delta r}{2}) = r_{i+1/2} = r_R$ and $(r - \frac{\Delta r}{2}) = r_{i-1/2} = r_L$. Similarly, the surface area on any given face, m , about a cell, i , can be computed from,

$$A_{i,m} = \iint r_{i,m}^2 \sin(\phi) d\theta d\phi = 4\pi r_{i,m}^2. \quad (42)$$

By expanding the first term on the right hand side of Equation (40) so that,

$$\frac{1}{\Delta V_i} \sum_{m=1}^2 \mathbf{n}_{i,m} \cdot \mathbf{F}_{i,m} A_{i,m} = \frac{1}{\Delta V_i} (\mathbf{n}_{i,1} \cdot \mathbf{F}_{i,1} A_{i,1} + \mathbf{n}_{i,2} \cdot \mathbf{F}_{i,2} A_{i,2}). \quad (43)$$

For simplicity and consistency, since we are only dealing with two faces where $m = 1$ corresponds to the left face and a subscript L and $m = 2$ corresponds to the right face and a

subscript R . By applying the area term we may now write Equation (43) as

$$\frac{1}{\Delta V_i} (\mathbf{n}_{i,L} \cdot \mathbf{F}_{i,L} A_{i,L} + \mathbf{n}_{i,R} \cdot \mathbf{F}_{i,R} A_{i,R}) = \frac{1}{\Delta V_i} (-4\pi \mathbf{F}_{i,L} r_L^2 + 4\pi \mathbf{F}_{i,R} r_R^2) .$$

By combining Equations (41), (42) and (43) and substituting back into Equation (40) we arrive at

$$\begin{aligned} \frac{d\mathbf{U}_i}{dt} &= \frac{4\pi \mathbf{F}_{i,L} r_L^2 - 4\pi \mathbf{F}_{i,R} r_R^2}{\frac{4\pi}{3} (r_R^3 - r_L^3)} + \mathbf{P}_i \\ &= \frac{3}{r_R^3 - r_L^3} (\mathbf{F}_{i,L} r_L^2 - \mathbf{F}_{i,R} r_R^2) + \mathbf{P}_i \\ &= \frac{-1}{\Delta r} (\alpha \mathbf{F}_{i,R} - \beta \mathbf{F}_{i,L}) + \mathbf{P}_i \end{aligned} \quad (44)$$

Where,

$$\alpha = \frac{3r_R^2}{r_L^2 + r_R r_L + r_R^2}, \quad \beta = \frac{3r_L^2}{r_L^2 + r_R r_L + r_R^2}, \quad \Delta r = r_R - r_L .$$

We could continue from this point with the physical source term \mathbf{P} , but to simplify the computational analysis it is advantageous to transform the governing equations to the Cartesian coordinate system so we can make use of the finite-volume method on Cartesian grids. In order to do this, we will introduce a geometric source term \mathbf{G} . To see where the geometric source term arises, one may rearrange Equation (36) so that,

$$\begin{aligned} \frac{\partial \mathbf{U}}{\partial t} + \frac{1}{r^2} \frac{\partial r^2 \mathbf{F}}{\partial r} &= \mathbf{P} \\ \frac{\partial \mathbf{U}}{\partial t} + \frac{2\mathbf{F}}{r} + \frac{\partial \mathbf{F}}{\partial r} &= \mathbf{P} \\ \frac{\partial \mathbf{U}}{\partial t} + \frac{\partial \mathbf{F}}{\partial r} &= -\frac{2\mathbf{F}}{r} + \mathbf{P} . \end{aligned}$$

By defining $\mathbf{G} = -\frac{2\mathbf{F}}{r}$, we have

$$\frac{\partial \mathbf{U}}{\partial t} + \frac{\partial \mathbf{F}}{\partial r} = \mathbf{G} + \mathbf{P}, \quad (45)$$

with

$$\mathbf{S} \equiv \mathbf{G} + \mathbf{P} = \begin{bmatrix} \frac{2k}{r} \frac{\partial T}{\partial r} \\ 0 \end{bmatrix} + \begin{bmatrix} \rho Q A M e^{-E/RT} \\ -\rho A M e^{-E/RT} \end{bmatrix}.$$

The del operator in Cartesian coordinates is given by,

$$\vec{\nabla}_C = \hat{i} \frac{\partial}{\partial x} + \hat{j} \frac{\partial}{\partial y} + \hat{k} \frac{\partial}{\partial z},$$

so that Equation (45) may be written clearly in divergence form as follows,

$$\frac{\partial \mathbf{U}}{\partial t} + \vec{\nabla}_C \cdot \mathbf{F} = \mathbf{S}. \quad (46)$$

We integrate Equation (46) and use the divergence theorem to arrive at

$$\frac{d}{dt} \int_V \mathbf{U} dV + \oint_S \mathbf{n} \cdot \mathbf{F} dS = \int_V \mathbf{S} dV. \quad (47)$$

Again, since we are in one dimension the average values for \mathbf{U} and \mathbf{S} can be expressed as

$$\begin{aligned} \bar{\mathbf{U}} &= \frac{1}{\Delta V} \int_{\Delta V} \mathbf{U} dV, \\ \bar{\mathbf{S}} &= \frac{1}{\Delta V} \int_{\Delta V} \mathbf{S} dV. \end{aligned}$$

Now, as before, substituting these average quantities into Equation (47) and dropping “-” for convenience, we have

$$\Delta V \frac{d\mathbf{U}}{dt} + \oint_S \mathbf{n} \cdot \mathbf{F} dS = \Delta V \mathbf{S}.$$

Putting the previous equation in semi-discrete form we arrive at

$$\frac{d\mathbf{U}}{dt} = \frac{-1}{\Delta V} \oint_S \mathbf{n} \cdot \mathbf{F} dS + \mathbf{S}.$$

As in the previous case, assuming a control volume about node i and having subscript L and R denote left and right faces while keeping in mind in the Cartesian system $A_{i,m}$ reduces to a point value and $\Delta V_i = \Delta x$

$$\begin{aligned} \frac{d\mathbf{U}_i}{dt} &= \frac{-1}{\Delta x} (\mathbf{n}_i \cdot \mathbf{F}_{i,L} + \mathbf{n}_i \cdot \mathbf{F}_{i,R}) + \mathbf{S}_i \\ &= \frac{-1}{\Delta x} (\mathbf{F}_{i,R} - \mathbf{F}_{i,L}) + \mathbf{S}_i. \end{aligned} \quad (48)$$

For the source term $\mathbf{S}_i = \begin{bmatrix} S_i \\ 0 \end{bmatrix}$ where,

$$\begin{aligned} S_i &= \left\langle \frac{dT}{dx} \right\rangle_i \frac{1}{\Delta x} \int_{\Delta x} \frac{2k}{x_i} dx + \frac{1}{\Delta x} \int_{\Delta x} \rho Q A M e^{-E/RT_i} dx \\ &= \left\langle \frac{dT}{dx} \right\rangle_i \frac{2k}{x_i \Delta x} \int_{\Delta x} dx + \frac{1}{\Delta x} \int_{\Delta x} \rho Q A M e^{-E/RT_i} dx \\ &= \left\langle \frac{dT}{dx} \right\rangle_i \frac{2k}{x_i} + \rho Q A M e^{-E/RT_i}. \end{aligned}$$

Note that $\langle \cdot \rangle$ denotes cell averages.

3.3. NUMERICAL ALGORITHM

To numerically express Equation (48) we will adopt the strategies developed by Gao et al. [35]. A primary goal will be to maintain fourth-order accuracy on the interior as well as the boundaries. As a result, two layers of ghost cells will be utilized. The values of the ghost cells are determined by extrapolating temperature information from the fuelbed and the physical boundary face. For the purposes of the following several equations we let i denote the location of the first ghost cell we are interested in and the subscript w denote the physical boundary face. The extrapolated values on the high-side of the domain (convection side) are given by,

$$\langle T \rangle_i = 4 \left(\langle T \rangle_w - \frac{1}{12} \langle T \rangle_{i-3} + \frac{5}{12} \langle T \rangle_{i-2} - \frac{13}{12} \langle T \rangle_{i-1} \right) \quad (49)$$

$$\langle T \rangle_{i+1} + \langle T \rangle_i = 4 \left(5 \langle T \rangle_w - \frac{2}{3} \langle T \rangle_{i-3} + \frac{37}{12} \langle T \rangle_{i-2} - \frac{83}{12} \langle T \rangle_{i-1} \right). \quad (50)$$

For the low-side of the domain (hotspot side),

$$\langle T \rangle_i = 4 \left(\langle T \rangle_w - \frac{1}{12} \langle T \rangle_{i+3} + \frac{5}{12} \langle T \rangle_{i+2} - \frac{13}{12} \langle T \rangle_{i+1} \right) \quad (51)$$

$$\langle T \rangle_{i-1} + \langle T \rangle_i = 4 \left(5 \langle T \rangle_w - \frac{2}{3} \langle T \rangle_{i+3} + \frac{37}{12} \langle T \rangle_{i+2} - \frac{83}{12} \langle T \rangle_{i+1} \right). \quad (52)$$

With the two ghost cells calculated, it is now possible to calculate fourth-order gradients near the boundaries as well as the interior using the same fourth-order scheme. In particular, to compute fourth-order, face-averaged temperature gradients the following centered stencil is employed,

$$\left\langle \frac{\partial T}{\partial x} \right\rangle_{i+\frac{1}{2}} = \frac{1}{12\Delta x} (-\langle T \rangle_{i+2} + 15\langle T \rangle_{i+1} - 15\langle T \rangle_i + \langle T \rangle_{i-1}). \quad (53)$$

For the source term, a fourth-order approximation for the cell-averaged derivative must be used and is given by,

$$\left\langle \frac{\partial T}{\partial x} \right\rangle_i = \frac{1}{12\Delta x} (-\langle T \rangle_{i+2} + 8\langle T \rangle_{i+1} - 8\langle T \rangle_{i-1} + \langle T \rangle_{i-2}). \quad (54)$$

3.3.1. INTERIOR SCHEME. As seen in the previous section, each interior cell has a source term and a flux component. Cell-averaged temperature gradients are required for computing the source term while face-averaged values are required for the flux term. For example, in our case the source term \mathbf{S} contains a cell-averaged temperature gradient which may be computed directly from Equation (54). We have,

$$\begin{aligned} \mathbf{S} &= \begin{bmatrix} \left\langle \frac{2k}{r} \right\rangle_i \left\langle \frac{\partial T}{\partial r} \right\rangle_i + \langle \rho Q A M e^{-E/RT} \rangle_i \\ \langle -\rho A M e^{-E/RT} \rangle_i \end{bmatrix} \\ &= \begin{bmatrix} \frac{2k}{12x_i\Delta x} (-\langle T \rangle_{i+2} + 8\langle T \rangle_{i+1} - 8\langle T \rangle_{i-1} + \langle T \rangle_{i-2}) + \rho Q A M e^{-E/R\langle T \rangle_i} \\ -\rho A M e^{-E/R\langle T \rangle_i} \end{bmatrix} \\ &= \begin{bmatrix} \frac{k}{6x_i\Delta x} (-\langle T \rangle_{i+2} + 8\langle T \rangle_{i+1} - 8\langle T \rangle_{i-1} + \langle T \rangle_{i-2}) + \rho Q A M e^{-E/R\langle T \rangle_i} \\ -\rho A M e^{-E/R\langle T \rangle_i} \end{bmatrix}. \end{aligned}$$

Similarly, the flux terms can be computed directly from the face-averaged values given by Equation (53) so that,

$$\mathbf{F}_{i+1/2} = \begin{bmatrix} \frac{-k}{12\Delta x} (-\langle T \rangle_{i+2} + 15\langle T \rangle_{i+1} - 15\langle T \rangle_i + \langle T \rangle_{i-1}) \\ 0 \end{bmatrix}.$$

Figure 3.3 illustrates the Cartesian grid used in the interior of the computational domain.

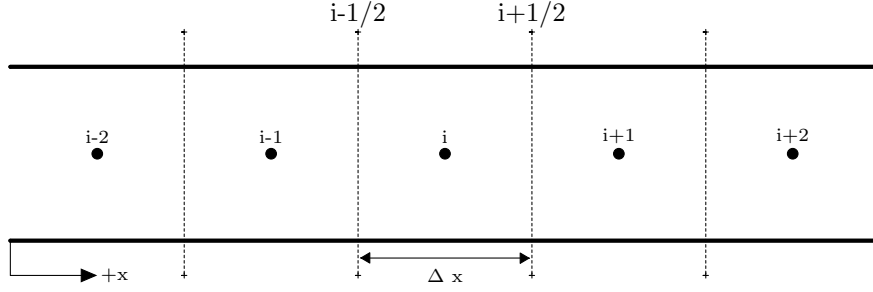


FIGURE 3.3. Cartesian grid for the biomass interior.

3.3.2. BOUNDARY SCHEME FOR LEFT HAND SIDE. In this model, we simulate a hot particle coming to rest in a fuelbed. The hotspot is to have an initial high temperature and will subsequently cool via conduction due to its contact with the low temperature fuelbed. We are not interested in resolving the temperature gradients in the hotspots domain from $0 \leq x < a$. Instead, the hotspot serves as a boundary condition at $x = a$ for the computational domain $a \leq x \leq b$. To obtain the temperature gradient on the physical boundary face, we need to solve a partial differential equation for the hotspot that depends on the thermal properties of the hotspot as well as the temperature values in the fuelbed. The following partial differential equation governs the temperature change of the hotspot:

$$\frac{\partial(\rho_H c_H T_H)}{\partial t} = \frac{\partial}{\partial x} \left(k_H x^2 \frac{\partial T_H}{\partial x} \right),$$

$$\text{Boundary Conditions: } \begin{cases} \frac{\partial T_H}{\partial r} \Big|_{r=0} = 0 \\ \frac{\partial T_H}{\partial r} \Big|_{r=a} = -k_f \frac{\partial T}{\partial r} \end{cases},$$

$$\text{Initial Conditions: } T(r, 0) = T_{H,Init}.$$

Since we are not concerned with resolving the temperature gradients within the hotspot itself, it is advantageous to solve for the hotspot boundary condition by taking a control volume analysis of the hotspot and using a lumped capacitance approach. For the hotspot-fuelbed interface for the sphere, the following will be used to justify this approach.

At the boundary between the fuel and the hotspot, heat due to conduction must be leaving the boundary at the same rate that it is entering thus,

$$\frac{4\pi k_H}{\frac{1}{r_1} - \frac{1}{r_2}}(T_{s,1} - T_{s,2}) = \frac{4\pi k_f}{\frac{1}{r_2} - \frac{1}{r_3}}(T_{s,2} - T_{s,3}).$$

Rearranging the above equation, we can define Bi_{cond} by

$$\text{Bi}_{cond} \equiv \frac{T_{s,1} - T_{s,2}}{T_{s,2} - T_{s,3}} = \frac{k_f}{k_H} \frac{(\frac{1}{r_1} - \frac{1}{r_2})}{(\frac{1}{r_2} - \frac{1}{r_3})}. \quad (55)$$

Note that subscript $(s, 1)$ corresponds to the center of the hotspot, $(s, 2)$ corresponds to the solid-solid interface, and $(s, 3)$ corresponds to the fuelbed-ambient boundary. Here the right hand side of the equation is analogous to the biot number if the hotspot was in contact with a fluid. We will assume that if this number is sufficiently small, $\text{Bi}_{cond} < 0.1$ then the lumped capacitance approach is an acceptable approximation. If $\text{Bi}_{cond} \geq 0.1$ then temperature gradients should be accounted for within the hotspot. Note that r_1 is approximately zero, but not equal to zero, to avoid a singularity. As a result, the hotspot at the boundary cools according to the following,

$$\rho_H V c_{p,H} \frac{dT_H}{dt} = k_f A \frac{dT}{dr} \Big|_{r=a}. \quad (56)$$

For a sphere of radius a , Equation (56) becomes,

$$\begin{aligned} \frac{dT_H}{dt} &= \frac{3k_f}{a\rho_H c_{p,H}} \frac{dT}{dr} \Big|_{r=a} \\ &= \frac{3k_f}{a\rho_H c_{p,H}} \frac{1}{12\Delta r} (-\langle T \rangle_{i+2} + 15\langle T \rangle_{i+1} - 15\langle T \rangle_i + \langle T \rangle_{i-1}) . \end{aligned} \quad (57)$$

In previous studies the constant power hotspot was analyzed [16, 17]. For this study it serves as a validation case. For this situation, the boundary condition is given as

$$-k \frac{\partial T}{\partial r} = \frac{P}{4\pi r_a^2}, \quad (58)$$

where P is the constant total power in watts and r_a is the radius of the hotspot. By using Equations (53) and (51), one can write Equation (58) in terms of the temperature on the boundary face T_w ,

$$T_w = \frac{1}{60} \left(\frac{12P\Delta r}{k4\pi r_a^2} + 80T_{i+1} + 5T_{i+3} - 26T_{i+2} + T_{i-1} \right) . \quad (59)$$

Figure 3.4 illustrates the Cartesian grid used on the hotspot-biomass boundary.

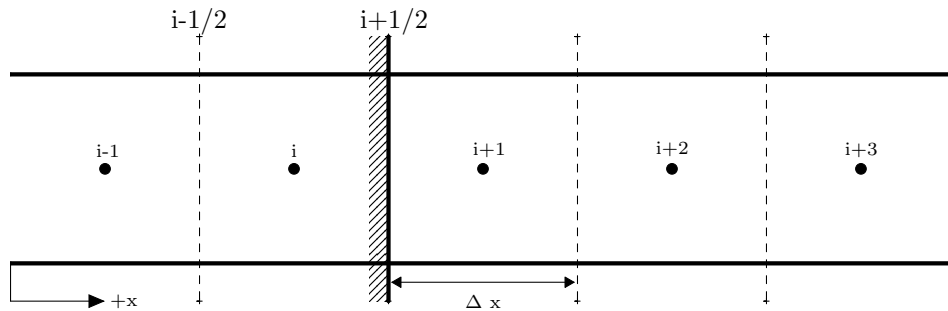


FIGURE 3.4. Cartesian grid for the hotspot-biomass boundary.

3.3.3. BOUNDARY SCHEME FOR RIGHT HAND SIDE. On the fuelbed-ambient interface the heat transfer occurs through convection only to an ambient temperature T_∞ . The convective boundary condition is written as,

$$k \left\langle \frac{\partial T}{\partial r} \right\rangle_{i+1/2} = h(T_\infty - \langle T \rangle_{i+1/2}).$$

Now through the discretization of this equation using Equation (53) we have,

$$\frac{k}{12\Delta r} (-\langle T \rangle_{i+2} + 15\langle T \rangle_{i+1} - 15\langle T \rangle_i + \langle T \rangle_{i-1}) = h(T_\infty - \langle T \rangle_{i+1/2}). \quad (60)$$

Rearranging and solving for $\langle T \rangle_{i+1/2}$

$$\langle T \rangle_{i+1/2} = -\frac{k}{12h\Delta r} (-\langle T \rangle_{i+2} + 15\langle T \rangle_{i+1} - 15\langle T \rangle_i + \langle T \rangle_{i-1}) + T_\infty. \quad (61)$$

Now substituting Equations (49) and (50), with appropriate indices, into the previous equation and letting $\langle T \rangle_w = \langle T \rangle_{i+1/2}$,

$$\langle T \rangle_w = \frac{k}{12h\Delta r} \left(\frac{170}{3} \langle T \rangle_i - \frac{46}{3} \langle T \rangle_{i-1} + \frac{8}{3} \langle T \rangle_{i-2} - 44 \langle T \rangle_w \right) + T_a.$$

Solving for $\langle T \rangle_w$,

$$\langle T \rangle_w = \frac{\frac{k}{12h\Delta r} \left(\frac{170}{3} \langle T \rangle_i - \frac{46}{3} \langle T \rangle_{i-1} + \frac{8}{3} \langle T \rangle_{i-2} \right) + T_\infty}{1 + (44k)/(12h\Delta r)},$$

Figure 3.5 illustrates the Cartesian grid for the biomass-ambient environment boundary.

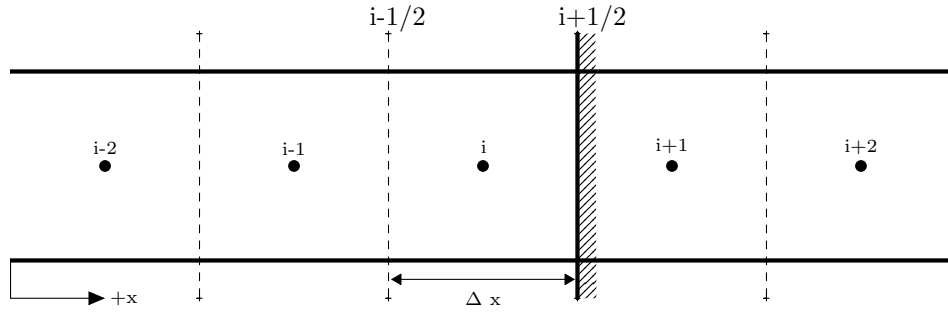


FIGURE 3.5. Cartesian grid for the biomass-ambient environment boundary.

CHAPTER 4

RESULTS AND DISCUSSION

4.1. NUMERICAL RESULTS

4.1.1. MODEL VERIFICATION. By using the parameter values from Staggs and Weber [15, 17] in Table 4.1, several numerical tests were investigated to verify and validate the numerical models. The test cases assume no mass loss and no heat generation. A constant temperature hotspot or a constant heat flux hotspot serves as the boundary condition on the left hand side while a constant temperature is used on the right hand side. As the

TABLE 4.1. Parameter values for the coupled reaction-diffusion system.

Fuel Parameter	Biomass	Hotspot
ρ [kg/m ³]	660	7500
c [J/kg·K]	750	434
k [W/m·K]	0.1	52
Q [J/kg]	5.7×10^5	-
A [1/s]	10^5	-
E [J/mol]	8.4×10^4	-

first test, we consider constant temperature boundaries with no source, the simplest case. An exact solution at steady state is known for our numerical model validation. In general, for spherical coordinates, the exact steady-state temperature profile under these conditions takes the form of

$$T(r) = \frac{C_1}{r} + C_2, \quad (62)$$

where the constants C_1 and C_2 are determined by the temperatures on the boundaries.

Figure 4.1 shows that the numerical solution approaches the exact steady-state solution. After long times the numerical solution matches the exact solution, which validates the numerical model.

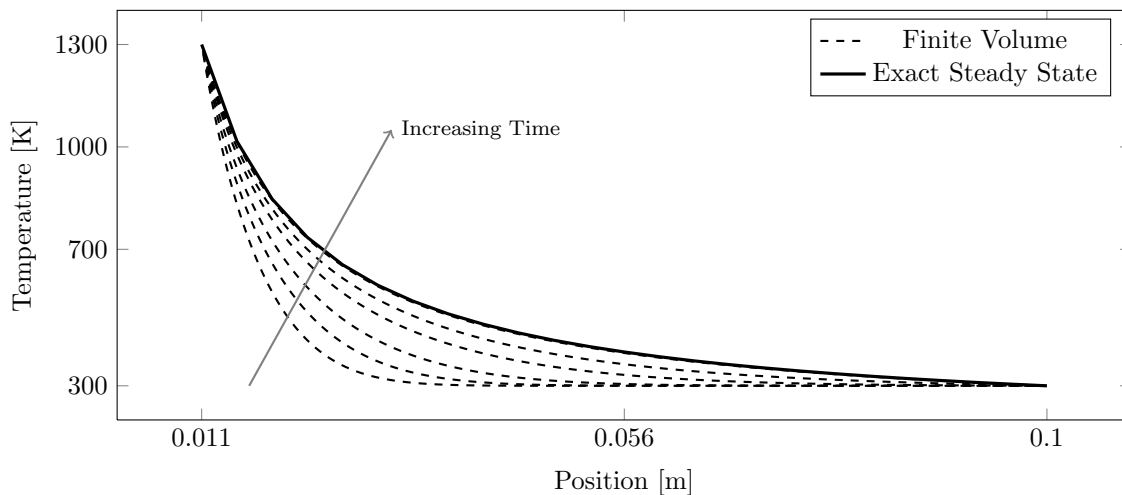


FIGURE 4.1. Finite-volume solution approaching the exact steady-state solution for constant temperature boundaries and no source term.

For a constant heat flux hotspot,

$$-k \frac{\partial T}{\partial r} \Big|_{r_a} = \frac{P}{4\pi r_a^2}, \quad (63)$$

using Equation (62) and applying the boundary conditions, the steady state solution takes the form,

$$T(r) = \frac{P}{4\pi k} \left(\frac{1}{r} - \frac{1}{r_b} \right) + T(r_b). \quad (64)$$

Here, P is the power of the hotspot in Watts. Figure 4.2 clearly shows $r_b = 0.05$ and $T(r_b) = 300$, and the numerical solutions approach the steady state over time, and eventually reaches the exact solution.

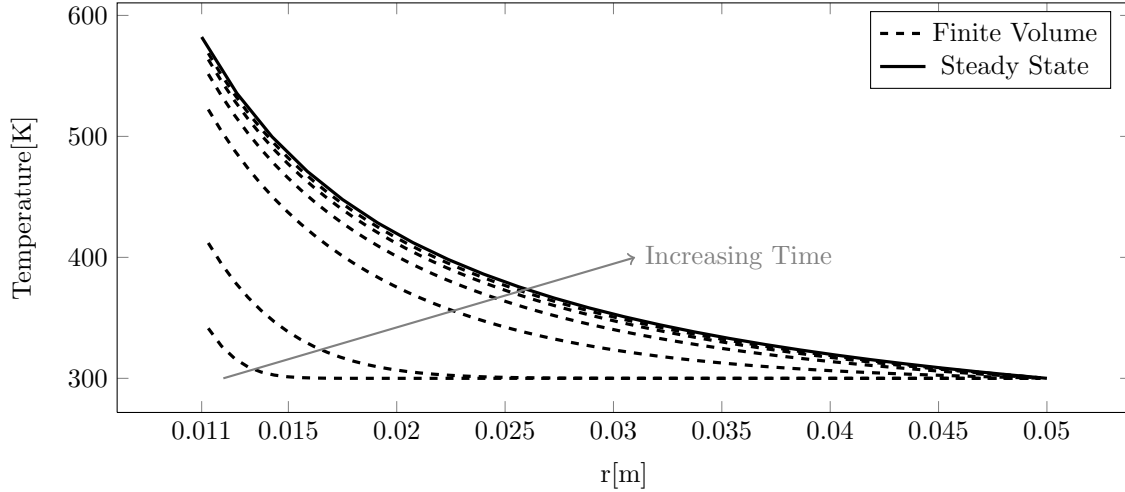


FIGURE 4.2. Finite-volume solution approaching the exact steady-state solution for a constant heat flux hotspot.

For a hotspot such as a bullet fragment coming to rest in a fuelbed of biomass, an initial temperature boundary condition is presumed to be the most realistic. It has been shown experimentally, and intuition suggests, that hot particles cool from an initial temperature to the temperature of the surroundings. Figure 4.3 shows that the system reaches an ambient temperature steady state after a sufficient amount of time has passed, which is as expected.

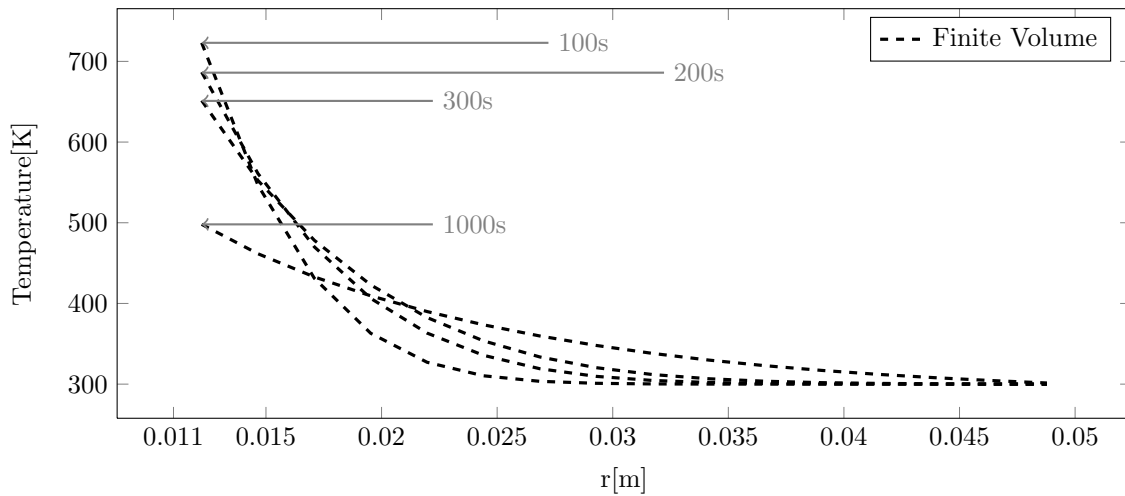


FIGURE 4.3. Finite-volume solution cooling to ambient temperature.

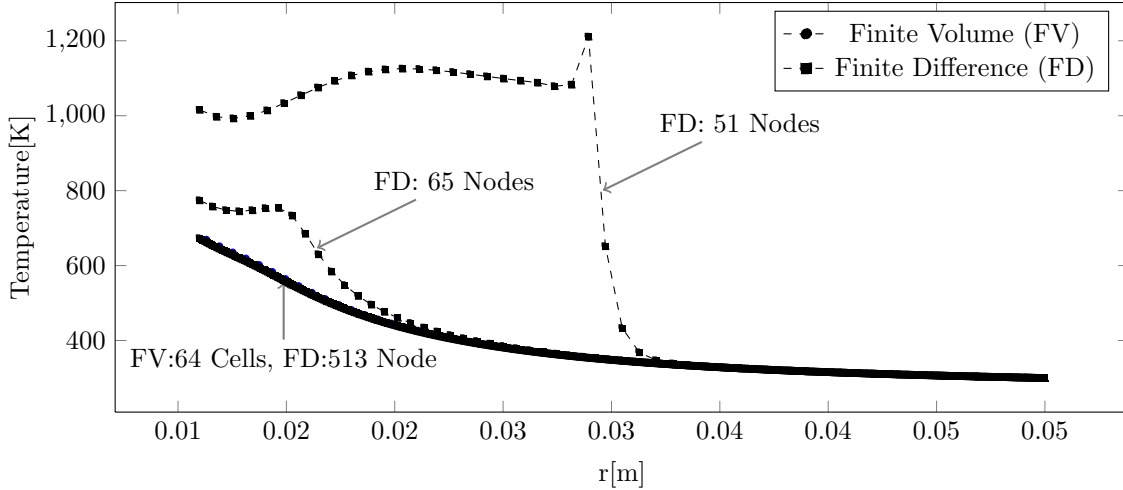


FIGURE 4.4. Grid study for a constant heat flux hotspot with the source term after 2000s.

Numerically, it is advantageous to use the finite-volume method to solve the coupled reaction-diffusion equations for several reasons. Since over or under estimating fuelbed temperatures can result in false ignitions or nonignitions, a fourth-order accurate numerical algorithm is desired. Moreover, the finite-volume method used in this work requires fewer nodes in contrast to the finite-difference method for the same solution error level. In addition, it is computationally efficient. For example, Figure 4.4 shows that for the constant heat flux boundary condition the finite difference approach requires a much finer grid size to match the finite volume method solution. It is also clear that in Figure 4.4 the finite difference method exhibits temperature profiles characteristic of ignitions at small grid sizes, but not at high spatial resolution. As the model is extended by the inclusion of more physics, the computational speed offered by the finite-volume approach will become important. Finally, the finite-volume method can be more easily extended to multiple dimensions in the spherical coordinate system. This would be useful if looking at other situations such as a partially embedded hotspot.

Figure 4.5 demonstrates a case that constitutes an ignition. At 10s it is apparent that enough energy was conducted from the hotspot to the fuelbed to overcome the activation energy resulting in the initialization of a combustion wave. Through times 30s, 50s, 70s and 90s, one can see the steadily propigating wave moving through the fuelbed until it reaches the fuelbed-ambient environment interface at around 200s. As the combustion wave moves through the fuelbed the mass fraction is zero up to current position of the combustion wave. As a result, after 200s the mass fraction is zero throughout the fuelbed. When the mass fraction is zero, the source term in the governing equations is zero as well and the fuelbed is then no longer capable of producing heat. As a result, the temperatures throughout the fuelbed begins to cool as shown at 300s and 500s. After more time the temperatures in the fuelbed would continue to decrease until ambient temperatures are reached everywhere. It is worth noting that the temperature of the fuelbed rises to an adiabatic temperature limit given by,

$$T_{adiabatic} = T_{ambient} + \frac{Q}{c_p}. \quad (65)$$

Figure 4.6 demonstrates a non-ignition case. In this figure, after 125s there is some heat release by the fuelbed which is reflected by a temperature profile with a slight bump. Since the mass fraction is zero up to this point, some combustion is occuring in the fuelbed. However, the heat release is not large enough for the initialization of a combustion wave. As the time goes from 500s to 4000s it is clear that the fuelbed temperature is approaching the ambient temperature. It is also clear that the mass fraction approaches a finite value over these times. Because not all of the fuel was consumed, this cannot constitute an ignition. In order to observe this non-ignition case the parameter Q was decreased. Physically, decreasing Q is analogous to increasing the moisture content of the fuelbed.

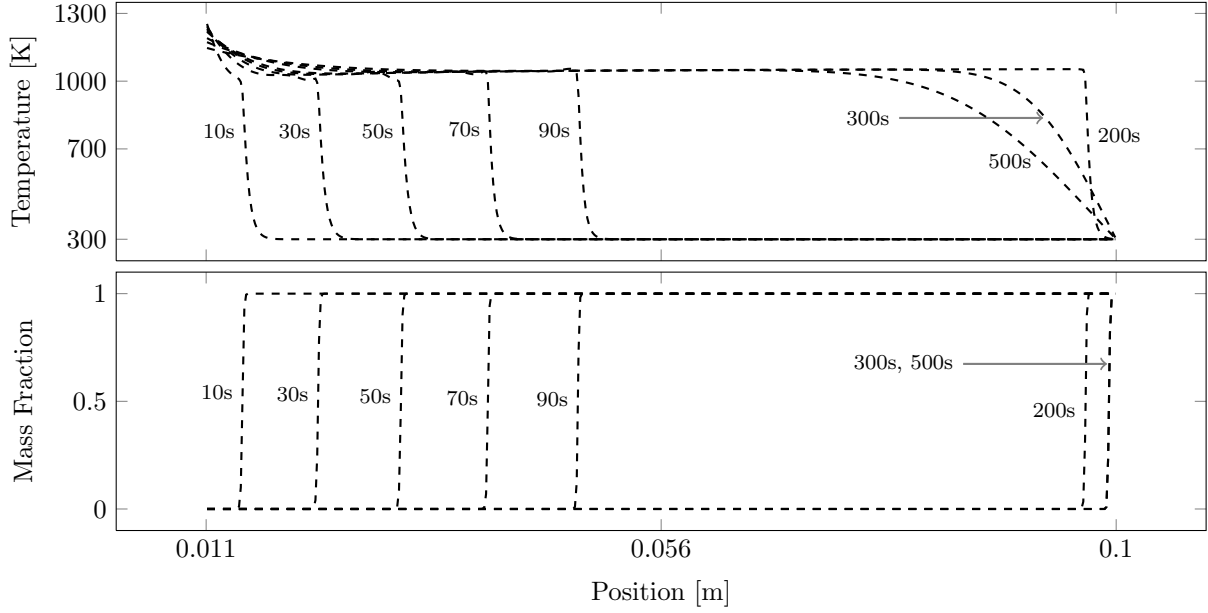


FIGURE 4.5. For a hotspot of radius $a = 0.011$ m and an initial temperature $T_H = 1300\text{K}$, an ignition is observed with $Q = 5.7 \times 10^5$ J/kg.

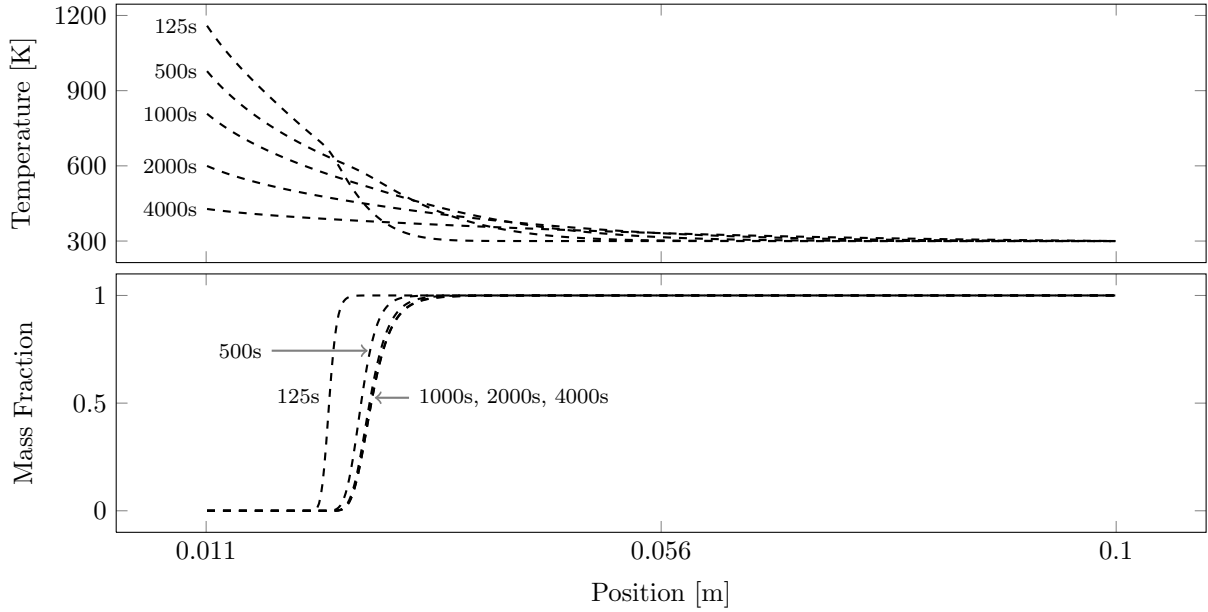


FIGURE 4.6. For a hotspot of radius $a = 0.011$ m and an initial temperature $T_H = 1300\text{K}$, an ignition does not occur with $Q = 4.9 \times 10^5$ J/kg.

By varying Q while keeping the other parameters fixed, there appears to be a critical Q value near 5×10^5 J/kg where the mass fraction goes to zero after 5000s for Q values greater

than the critical value. Increasing Q , explosion occurs at around $Q = 9.4 \times 10^5$. Figure 4.7 illustrates the full extent of combustion after 5000s demonstrating the existence of a critical Q value.

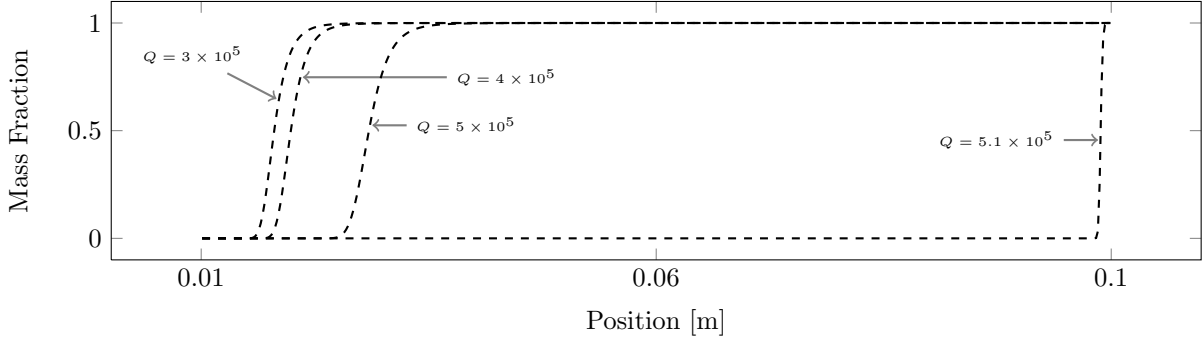


FIGURE 4.7. After 5000 s the total extent of combustion shows that an ignition occurs for $Q > 5 \times 10^5$ J/kg.

From the numerical solutions given in the previous section, a clear characteristic of a non-ignition is the failure to produce a combustion wave. A result of this is the total mass fraction of the biomass approaches some non-zero value as show in Figure 4.6. By subtracting the current mass fraction solution from the mass fraction solution at the next time, Figure 4.8 shows that over time the numerical solutions converge. In Figure 4.8, ΔM_{t_1} is the solution difference from 125-250s, ΔM_{t_2} is the solution difference from 250-500s, ΔM_{t_3} is the solution difference from 500-1000s, ΔM_{t_4} is the solution difference from 1000-2000s, and ΔM_{t_4} is the solution difference from 2000-4000s. Certainly, convergence of mass fraction solutions alone is not enough to determine an ignition since, in both ignition and non-ignition cases, ΔM goes to zero. In order to quantify the extent of the converged solution a strategy proposed by Staggs [15] is adopted. Using the L_2 norm given by

$$\|M\|_2 = \sqrt{\int_a^b M^2 dr}, \quad (66)$$

if $\|M\|_2$ approaches a nonzero value as ΔM approaches zero then an ignition did not occur in the biomass. Following Staggs [15] we may assume that after ten biomass diffusion time scale if $\|M\|_2$ is less than 10^{-10} , the biomass is fully burnt. Staggs also defined the biomass diffusion time scale as $\rho_f c_f b^2 / k_f$. Allowing the numerical solver to run for ten biomass diffusion timescale lengths would guarantee that the solution has converged to its steady-state solution.

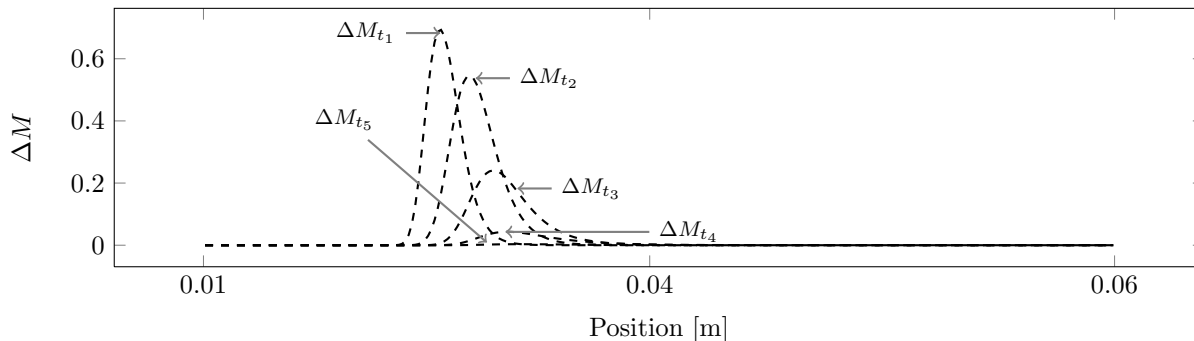


FIGURE 4.8. Convergence of mass fraction solutions from Figure 4.6.

4.2. DISCUSSION

By looking at the dimensionless form of the governing equations using the Frank-Kamenetskii critical δ_c while ignoring mass loss, two possible states can be defined, namely an ignition state or a non-ignition state. If the heating parameter, δ , is above the critical value, the ignition state, temperatures always approach infinity. In the non-ignition state, temperatures always approach a finite value as time increases. To include moisture content we vary the heat release and specific heat based on a probability distribution around average moisture content values up to 30%. A good correlation can be made to the CEMML ignition data using a simple ignition criteria based on Gol'dshleger's hotspot theory and the moisture dependent biomass parameters. However, such a simple model only works by carefully calibrating parameters, such as the pre-exponential constant and moisture distribution.

Nevertheless, this simple model can provide reasonable predictions for the longleaf pine, but does not for cheatgrass or smoothbrome. This suggests that the Gol'dshleger hotspot ignition model is more qualitative than quantitative. Therefore, adding additional physics, such as mass loss, to Gol'dshleger's hotspot model should improve the predictability. Furthermore, incorporating additional physics allows for more realistic ignition criteria. For every ignition observed in this work, a combustion wave propagated throughout the fuelbed at a constant rate without interruption and results in satisfying a common criteria. This criteria is the measure of the fuel mass over a characteristic time length given by $\rho_f c_f b^2 / k_f$. A more precise criteria for ignition is, perhaps, the onset of a combustion wave. It also appears that heating values may be explored as an ignition criteria. It is found that the numerical model requires reasonable values of the physical and thermodynamic properties of the biomass. Specifically, if reasonable values are not used, temperatures can approach infinite values. In Figure 4.7 solutions were not obtained if Q was approximately 9.4×10^5 J/kg. However, the problem is that there is a significant uncertainty in property estimations for biomass. In addition, the convection is not included in the numerical model. Heat release due to combustion is not being convected out of the system effectively. Furthermore, oxygen diffusion, porosity of the fuelbed, and radiation effects within the fuelbed have been neglected. It is also observed that by reducing the radius of the fuelbed, the quick burnout of the fuel results in the convective boundary condition becomes more effective at earlier times resulting in faster cooling and more realistic exothermic behaviors exhibited by the biomass.

CHAPTER 5

CONCLUSION AND FUTURE WORK

We have shown that a correlation can be developed between experimental ignition data using a simplified, non-dimensional model with critical values found by Gol'dshleger et al. It was established that the bifurcation-point that differentiates thermal explosion and steady-state solutions provides a basic ignition criteria that can be compared with more complex ignition models. Next, we have demonstrated that the numerical solution to the coupled reaction-diffusion equations allows us to use mass loss as an ignition criteria. By including the effects of mass loss governed by a first-order, Arrhenius reaction, issues arise when biomass parameter values from Chapter 1 are used. A result of this is unreasonable adiabatic temperature values, as well as thermal explosion behavior that was also seen in the simplified, non-dimensional model. It is clear that the uncertainty in these parameter values for longleaf pine, cheatgrass, and smooth brome results in inaccurate analysis for these specific biomass species. Moreover, some experimental work is needed to better understand the combustion properties of the specific biomass being studied with an emphasis on the activation energy and the pre-exponential constant. Additional experimental work can be done to validate the coupled reaction-diffusion model. Future work is needed to determine what range of parameters are possible that allow for a steady-state solution, the onset of a combustion wave, or thermal explosion for the coupled reaction-diffusion system. Capturing more physics, such as oxygen diffusion, and taking into account the porosity of the biomass is thought to allow for more realistic parameters without resulting in thermal explosion. A next step for the ignition model will be to account for oxygen diffusion so that all of the primary factors that are necessary for ignition (fuel, heat source, and oxidizer) will be fully accounted for

in the governing equations. With more accurate biomass parameters, and the inclusion of oxygen diffusion, the ignition criteria described in Chapter 4 should result in a more accurate correlation to biomass ignition data.

BIBLIOGRAPHY

- [1] E. Pastor, L. Zarate, E. Planas, and J. Arnaldos, “Mathematical models and calculation systems for the study of wildland fire behaviour,” *Progress in Energy and Combustion Science*, vol. 29, no. 2, pp. 139–153, 2003.
- [2] E. Koo, P. J. Pagni, D. R. Weise, and J. P. Woycheese, “Firebrands and spotting ignition in large-scale fires,” *International Journal of Wildland Fire*, vol. 19, no. 7, pp. 818–843, 2010.
- [3] N. Sardoy, J.-L. Consalvi, B. Porterie, and A. C. Fernandez-Pello, “Modeling transport and combustion of firebrands from burning trees,” *Combustion and Flame*, vol. 150, no. 3, pp. 151–169, 2007.
- [4] V. Babrauskas, *Ignition Handbook*. Issaquah, WA 98027: Fire Science Publishers, 2003.
- [5] S. McAllister, M. Finney, and J. Cohen, “Critical mass flux for flaming ignition of wood as a function of external radiant heat flux and moisture content,” *7th US National Technical Meeting of the Combustion Institute*, 2011.
- [6] G. Rowntree and A. Stokes, “Fire ignition by aluminum particles of controlled size,” *Journal of Electrical and Electronics Engineering Australia*, vol. 14, p. 117, 1994.
- [7] C. J. Rallis and B. M. Mangaya, “Ignition of veld grass by hot aluminum particles ejected from clashing overhead transmission lines,” *Fire Technology*, vol. 38, pp. 81–92, 2002.
- [8] D. T. Stephen and A. C. Fernandez-Pello, “On the flight paths of metal particles and embers generated by power lines in high winds a potential source of wildland fires,” *Fire Safety Journal*, vol. 30, no. 4, pp. 333–356, 1998.

- [9] R. M. Hadden, S. Scott, C. Lautenberger, and A. C. Fernandez-Pello, “Ignition of combustible fuel beds by hot particles: An experimental and theoretical study,” *Fire Technology*, vol. 47, pp. 341–355, 2011.
- [10] J. L. Urban, C. D. Zak, and C. Fernandez-Pello, “Cellulose spot fire ignition by hot metal particles,” *Proceedings of the Combustion Institute*, vol. 35, pp. 2707–2714, 2015.
- [11] A. Fernandez-Pello, C. Lautenberger, D. Rich, C. Zak, J. Urban, R. Hadden, S. Scott, and S. Fereres, “Spot fire ignition of natural fuel beds by hot metal particles, embers, and sparks,” *Combustion Science and Technology*, vol. 187, no. 1-2, pp. 269–295, 2015.
- [12] M. A. Finney, T. B. Maynard, S. S. McAllister, and I. J. Grob, “A study of ignition by rifle bullets,” tech. rep., RMRS-RP-104. Fort Collins, CO: US Department of Agriculture, Forest Service, Rocky Mountain Research Station, 2013.
- [13] J. R. Hall, *The Total Cost of Fire in the United States*. National Fire Protection Association, 2014.
- [14] A. M. Beavers and C. M. Herron, “The tracer ignition minimization (tim) tool,” tech. rep., Project 10-374, Department of Defense Legacy Program, 2012.
- [15] J. E. Staggs, “A theoretical investigation of initiation of travelling combustion fronts in fuel beds from embedded hotspots,” *Journal of Fire Sciences*, vol. 30, no. 5, pp. 437–456, 2012.
- [16] J. Brindley, J. Griffiths, and A. McIntosh, “Ignition phenomenology and criteria associated with hotspots embedded in a reactive material,” *Chemical Engineering Science*, vol. 56, pp. 2037–2046, 2001.

- [17] R. Weber, H. Sidhu, D. Sawade, G. Mercer, and M. Nelson, “Using the method of lines to determine critical conditions for thermal ignition,” *Journal of Engineering Math*, vol. 56, pp. 185–200, 2006.
- [18] U. Gol’dshleger, K. Pribytkova, and V. Barzykin, “Ignition of a condensed explosive by a hot object of finite dimensions,” *Translated from Fizika Goreniya i Vzryva*, vol. 9, pp. 119–123, 1973.
- [19] D. A. Frank-Kamenetskii, *Diffusion and heat exchange in chemical kinetics*. Plenum Press, 2nd ed., 1969.
- [20] K. Ragland, D. Aerts, and A. Baker, “Properties of wood for combustion analysis,” *Bioresource Technology*, vol. 37, pp. 161–168, 1991.
- [21] K. W. Ragland and K. M. Bryden, *Combustion Engineering*. 6000 Broken Sound Parkway NW, Suite 300: Taylor and Francis Group”, 2nd ed., 2011.
- [22] C. Dupont, R. Chiriac, G. Gauthier, and F. Toche, “Heat capacity measurements of various biomass types and pyrolysis residues,” *Fuel*, vol. 115, pp. 644–651, 2014.
- [23] J. Jones, “Oven heating tests for propensity to self-heating,” *Combustion and Flame*, vol. 124, pp. 334–336, 2001.
- [24] N. Y. Harun and M. T. Afzal, “Thermal decomposition kinetics of forest residue,” *Journal of Applied Sciences*, vol. 10 (12), pp. 1122–1127, 2010.
- [25] J. H. Flynn and L. A. Wall, “A quick, direct method for the determination of activation energy from thermogravimetric data,” *Polymer Letters*, vol. 4, pp. 323–328, 1966.
- [26] ASTM E1641-13, “Decomposition kinetics by thermogravimetry using the ozawa/flynn/wall method,” tech. rep., ASTM International, West Conshohocken PA, 2013. www.astm.org.

- [27] P. McKendry, “Energy production from biomass (part 1): overview of biomass,” *Biore-source Technology*, vol. 83, pp. 37–46, 2002.
- [28] P. Lam, S. Sokhansanj, X. Bi, C. Lim, L. Naimi, M. Hoque, S. Mani, A. Womac, X. Ye, and S. Narayan, “Bulk density of wet and dry wheat straw and switchgrass particles,” *Applied Engineering in Agriculture*, vol. 24, pp. 351–358, 2008.
- [29] P. Santoni, P. Bartoli, A. Simeoni, and J. Torero, “Bulk and particle properties of pine needle fuel beds - influence on combustion,” *International Journal of Wildland Fire*, vol. 23, pp. 1076–1086, 2014.
- [30] F. P. Incropera, P. DeWitt David, T. L. Bergman, and A. S. Lavine, *Fundamentals of Heat and Mass Transfer*. John Wiley and Sons, 6th ed., 2006.
- [31] A. Atreya, “Ignition of fires,” *Philisophical Transactions: Mathematical, Physical and Engineerig Sciences*, vol. 356, pp. 2787–2813, 1998.
- [32] L. Yarin, *The Pi-Theorem: Applications to Fluid Mechanics and Heat and Mass Transfer*, vol. 1. Springer Science and Business Media, 2nd ed., 2012.
- [33] T. Boddington, P. Gray, and D. Harvey, “Thermal theory of spontaneous ignition: Criticality in bodies of arbitrary shape,” *Philosophical Transactions of the Royal Society of London. Series A, Mathematical and Physical Sciences*, vol. 270, no. 1207, pp. 467–506, 1971.
- [34] P. Thomas, “On the thermal conduction equation for self-heating materials with surface cooling,” *Transactions of the Faraday Society*, vol. 54, pp. 60–65, 1958.
- [35] X. Gao, S. Guzik, and P. Colella, “A fourth-order boundary treatment for viscous fluxes on cartesian grid finite-volume methods,” *American Institute of Aeronautics and Astronautics*.